Aeroacoustic Prediction of Overwing Propulsion at Incidence

Hasse N. J. Dekker* and Marthijn Tuinstra†
Royal Netherlands Aerospace Centre, 8316 PR Marknesse, The Netherlands
and
Daniele Ragni‡
Delft University of Technology, 2629 HS Delft, The Netherlands

https://doi.org/10.2514/1.J064986

The premise of over-the-wing mounted rotors is that a favorable aerodynamic effect is achieved by interaction with the lifting wing, which also acts as noise shield. A physics-based low-order model is proposed that accounts for aerodynamic interactions in the prediction of the aeroacoustic footprint of the installed rotor. The nonuniform inflow of the rotor disk is modeled by an analytical description of the inviscid potential effects of the wing's circulation, given as a function of the blade sectional coordinates. Furthermore, the ingestion of the separated boundary layer is considered at large angles of attack. The related steady inflow distortion serves as input to an aeroacoustic noise prediction chain that computes the unsteady loading on the blades and the resulting tonal noise emission by helicoidal surface theory. The model is validated by measurements from a single over-the-wing mounted rotor for a wide range of angle of attack, advance ratios, and rotor positions over the wing's chord. The predictions and experimental data show an equivalent increase in the tonal components relative to the isolated rotor, and a minimization of the tonal noise for a midchord rotor position, for emission directions around the rotor disk plane over the wing's suction side.

Nomenclature

B	=	number of blades
c	=	wing chord, m
c_l	=	two-dimensional lift coefficient, equal to $L/(qcS)$
c_0	=	speed of sound, m^{-1}
C_p	=	pressure coefficient, equal to $(p - p_\infty)/q$
C_{SL}	=	shear-layer correction term
$\hat{C}_L$	=	complex two-dimensional lift coefficient
$\hat{C}_D$	=	complex two-dimensional lift coefficient
C_T	=	thrust coefficient, equal to $T/(\rho n^2 D^4)$
C'_T	=	sectional thrust coefficient thrust coefficient, equal to $T'/(\rho n^2 D^3)$
C_Q	=	torque coefficient, equal to $Q/(\rho n^2 D^5)$
C'_Q	=	sectional thrust coefficient thrust coefficient, equal to $Q'/(\rho n^2 D^4)$
D	=	rotor diameter, m
$\hat{H}$	=	complex normalized thickness of the displaced fluid
J	=	rotor advance ratio, equal to $V_\infty/(nD)$
$\hat{J}_n$	=	Bessel function of the nth order
k	=	wave number, m^{-1}
M	=	Mach number
M_x	=	flight Mach number
n	=	shaft frequency, Hz
q	=	freestream dynamic pressure, Pa
Q	=	rotor torque, Nm
R	=	radial coordinate
R_0	=	rotor inner radius, m
R_1	=	rotor outer radius, m
Re_c	=	chord-based Reynolds number
R_{bc}	=	blade chord-based Reynolds number
$\hat{S}$	=	Sear's function
T	=	rotor thrust, N
$\hat{t}_b$	=	complex blade thickness, m
t_{SL}	=	shear-layer thickness, m
V	=	velocity magnitude, m/s
X	=	normalized blade chord coordinates, equal to $x/c - 1/2$
x_r	=	x position of the rotor tip from wing's leading edge, m
y_o	=	y position of far-field observer, m
y_r	=	y position of the rotor shaft from wing's surface, m
y_{SL}	=	shear-layer height, m
y_t	=	rotor tip gap from wing's surface, equal to $y_r - R_1$, m
α	=	geometric angle of attack, deg
α_0	=	blade's trailing-edge separation angle, rad
α_1	=	blade's leading-edge separation angle, rad
α_{eff}	=	effective angle of attack, rad
α_c	=	stall angle, rad
β	=	blade pitch angle, rad
θ	=	azimuthal coordinate, rad
θ_o	=	far-field observer position, rad
λ	=	wavelength of one BPF, equal to c_0/BPF, m
BPF	=	blade passing frequency, Hz
ρ	=	density of air, kg/m^3
σ	=	reduced frequency
σ_{SL}	=	shear-layer spreading coefficient
τ	=	tracer particle relaxation time, s
ϕ_0 and ϕ_s	=	phase lag due to blade offset and blade sweep
$\psi_{V,n}$, $\psi_{L,n}$, and $\psi_{D,n}$	=	normalized thickness, lift, and drag source transforms
Ω	=	shaft frequency, equal to, $2\pi n$, rad/s

Subscripts

ax	=	axial direction
e	=	outlet stream tube condition
iso	=	isolated rotor conditions
QS	=	quasi-steady condition
r	=	condition at radial position

Received 15 October 2024; accepted for publication 25 March 2025; published online 26 June 2025.

*Ph.D. Candidate, Vertical Flight and Aeroacoustics Department; hasse.dekker@nlr.nl. Member AIAA.
†Head of Department, Vertical Flight and Aeroacoustics Department; marthijn.tuinstra@nlr.nl. Member AIAA.
‡Associate Professor, Wind Energy, Faculty of Aerospace Engineering; d.ragni@tudelft.nl. Member AIAA.

t = blade tip condition
∞ = freestream condition
θ = azimuthal direction

I. Introduction

TILT-WING vertical takeoff aircraft configurations provide a promising vehicle architecture because they combine the maneuverability of a helicopter with the cruise efficiency of an aircraft [1,2]. These configurations often make use of tight integration of fixed-pitched rotors with aerodynamic surfaces [3], aiming at beneficial aerodynamic coupling to increase the aircraft's efficiency. Integration of the propulsion system alters the acoustic signature of an isolated rotor in three ways. First of all, variations in blade loading along the rotor's azimuth are expected by the aerodynamic interference with the mean flow of wings and pylons, leading to additional noise sources from the rotor [4]. Second, when located in the vicinity of a surface, wave reflection, diffraction, and absorption effects might occur [5,6], changing the directivity patterns along the aircraft. Finally, the turbulent wake and tip vortices of the rotor can interact with downstream surfaces, resulting in additional sources of noise [7,8].

Over-the-wing propulsion [9–11] is a conceptual configuration where such aeropropulsive and acoustic installation effects are encountered. In this layout, the rotors are positioned on the suction side of the wing with their axes aligned with the wing's chord line; see Fig. 1. This placement allows shielding of rotor noise to reduce flyover noise [12–14]. A second benefit is that an over-the-wing configuration can lead to increased aerodynamic efficiency [10,11]. Rotor-induced flow causes a lift increase, dependent on the angle of attack and the chordwise position of the rotor relative to the wing. Additionally, reductions in drag have also been reported in the literature [15]. In a recent investigation by de Vries and Vos [16], it was shown that these benefits translate to an enhanced aerodynamic efficiency of 9% and reduced energy consumption of 5% (although with an uncertainty of 5%) on the aircraft level, compared to a twin-turboprop reference vehicle.

Although the wing's shielding offers an evident acoustic advantage, aerodynamic wing-interference effects generate additional noise sources. The rotor wake increases turbulence fluctuations over the wing [17], and hence broadband noise by trailing edge scattering. More substantive is the effect of nonuniform rotor disk inflow due to the presence of the wing [17]. Consequently, blade loading variations are incurred as a function of the rotor azimuth angle [18], increasing the tonal noise amplitudes at the higher harmonics of the blade passing frequency [19]. For moderate to large angles of attack, typically experienced when transitioning from vertical to cruise operation [2], the boundary layer separates [20], leading to strongly distorted mean inflow. The ingestion of turbulence from the separated boundary layer additionally increases broadband noise levels [21]. Finally, the pressure jump over the rotor disk leads to an adverse pressure gradient enhancing boundary-layer ingestion, which is lifted into the rotor disk. The isolated effect was studied by Murray et al. [22] for a propeller positioned above a flat plate, ingesting a turbulent boundary layer.

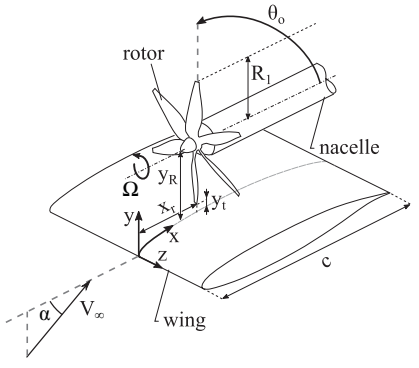

Fig. 1 Schematic representation of the over-the-wing rotor with relevant parameters and system of coordinates; θ_O presents the rotor emission direction.

The use of low-fidelity tools allows for efficient optimization of the propulsion system and is therefore particularly useful for minimizing the adverse effects on the aerodynamic noise sources of the rotor. Foundation for far-field tonal noise predictions of propellers was presented in the early work of Gutin [23]. The physical understanding behind the noise generation was generalized by the Ffowcs Williams and Hawkings analogy [24–26], dealing with solid bodies in motion in a uniform reference medium, in which sources due to fluid displacement, blade forces, and flow inhomogeneities surrounding the blades were incorporated. This theory paved the way for efficient and reliability analytical propeller tonal noise models, such as Hanson's helicoidal surface theory [27], which included additional corrections for blade thickness and sweep. Aforementioned methods are derived under the assumption of uniform inflow conditions. Recent studies have included adaptations to account for unsteady loading in various configurations, including pusher propellers [28,29], quadrotors [30], contrarotating open rotors [31], and distributed propellers [32]. The noise ascribed to unsteady loading was shown to be dominant for most noise emission angles for such configurations [30], highlighting its relevance. Analytical predictions of acoustic installation effects have also received recent attention, such as shielding properties [33] and edge diffraction effects [5] caused by the close positioning of propellers to wings.

1. *Present Contribution and Outline*

Noise models and acoustic guidelines for over-the-wing rotors are lacking in the public domain. In the present work, a low-fidelity acoustic model is proposed and used to investigate the effect of the rotor–wing performance and geometric parameters. For the acoustic predictions, an aerodynamic inflow model is used to estimate the unsteady loading of the blades. Information on the loading is then used to compute the far-field acoustics using helicoidal surface theory. The proposed model focuses on tonal the noise emissions of the installed rotor, and therefore the shielding and scattering effects of the wing's surface are disregarded. Predictions are validated against measurements of a single over-the-wing mounted rotor.

The outline of the paper is as follows. In Sec. II, the performance and acoustic modeling techniques are introduced and Sec. III deals with the experimental setup. In Sec. IV, the aeroacoustic characteristics of the rotor–wing system are elucidated based on experimental results. Flow regimes excluded in the model are identified, and the relative importance of tonal and broadband noise is quantified. Finally, in Sec. V, the model results are compared to the measurements, and a parametric study is performed on the chordwise rotor position.

II. Tonal Noise Modeling Techniques

The modeling approach accounts for the wing's influence on the rotor loads by considering the flow pattern over the isolated wing. This includes the inviscid flow acceleration due to circulation and separated boundary-layer ingestion at high angles of attack, analogous to the steady-thrust model for over-the-wing propulsion [20]. The formulation incorporates nonuniform and nonaxial inflow at the rotor disk, see Fig. 2a, required to obtain the rotor azimuth-dependent blade loading. In the initial step, the contributions of the inviscid and viscous flow features are modeled for both the axial V_x and nonaxial velocity V_y as a function of the wing-normal coordinate y, for a given rotor position (x_r, y_r). Then, the inflow velocity components $V_x(y)$ and $V_y(y)$ are transferred to the cylindrical coordinate frame (θ, R) of the rotor disk; see Fig. 2b. For a full rotation, the axial $V_{\mathrm{ax}}(\theta, R)$ and tangential $V_\theta(\theta, R)$ inflow velocity is prescribed at each blade section; see Fig. 2c. This includes the local rotational velocity of the blade section itself as well. The derivations of the axial $V_{\mathrm{ax}}(\theta, R)$ and tangential $V_\theta(\theta, R)$ velocities are shown in Secs. II.A and II.A, respectively.

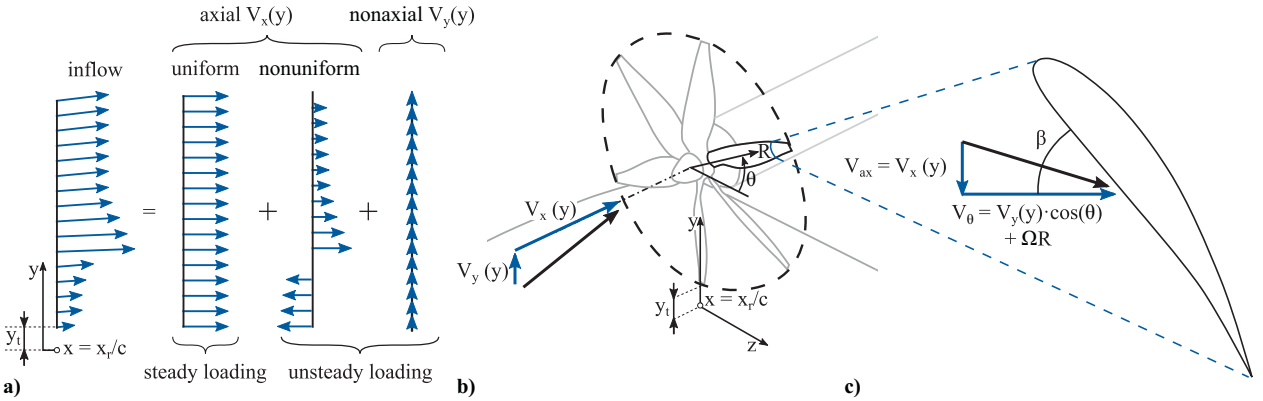

Fig. 2 Schematic representation of rotor velocity components: a) decomposition of the inflow at the rotor position (x_r, y_r), b) horizontal V_x and vertical velocity V_y components at the rotor's inflow, and c) definition of axial V_{ax} and tangential velocity V_θ of the blade section at (θ, R).

A. Axial Inflow Velocity

1. Inviscid: Circulation

The axial induced velocity by the wing's circulation is computed by integration of Biot-Savart's law [34]. This states that the local induced velocity in a reference point $\boldsymbol{r}$ by a set of discretized vortex filaments reads:

$$\boldsymbol{V}_\Gamma(\boldsymbol{r}) = \int_s \frac{\Gamma(\boldsymbol{s})}{4\pi} \frac{\boldsymbol{s}\times\boldsymbol{r}}{|\boldsymbol{r}|^3}\,\mathrm{d}\boldsymbol{s} \tag{1}$$

in which Γ and $\boldsymbol{s}$ denote the strength and location of the vortex filaments, respectively. By thin airfoil theory and assuming a parabolic source strength distribution of bound vortex filaments along the wing's chord, see Fig. 3a, the distribution of circulation Γ in chordwise direction x is written as a function of the wing's lift coefficient c_l:

$$\Gamma(x) = \frac{3}{4} c_l V_\infty c\left(1 - \frac{x^2}{c^2}\right) \tag{2}$$

Substituting Eq. (2) in Eq. (1), and transferring to blade coordinates, reduces the equation for the axially induced velocity $V_{x,\Gamma}$ at the rotor's disk to

$$V_{x,\Gamma}(R,\theta) = \frac{1}{2\pi}\int_0^c \frac{\Gamma(x)(y_r + R\sin\theta)}{(x_r - x)^2 + (y_r + R\sin\theta)^2}\,\mathrm{d}x \tag{3}$$

which can be solved analytically; see Appendix A for the final form.

2. Viscous: Shear-Layer Ingestion

At a critical angle of attack α_c (found by using an empirical relation as a function of the wing's nose radius to chord length r_c/c [35]), the wing's boundary layer separates at the leading edge. The shear-layer height y_{SL} is modeled by a linear function parallel to the freestream direction (see Fig. 3b),

$$y_{SL}(x) = x\,\tan(\alpha) \tag{4}$$

and imposes a jump in velocity when a blade section enters the separated flow region. The blade section transitioning into the separated flow region is modeled by an approximation of the Heaviside step function h in which the slope corresponds to the shear-layer thickness t_{SL}, as is shown in Fig. 3c,

$$h(R,\theta) = \frac{1}{1 + e^{-c_1\left(\frac{y_{SL}(x_r)}{y_r + R\sin\theta} - 1\right)}}, \quad c_1(x_r) = \frac{2R_1\,\ell n\left(\frac{1}{0.99} - 1\right)}{t_{SL}(x_r)} \tag{5}$$

in which c_1 is a coefficient based on the shear-layer thickness t_{SL}; see Fig. 3b. Using the self-similar solution of Görtler [36] describing a planar free shear layer, the thickness t_{SL} can be approximated by [37]

$$t_{SL}(x_r) = \frac{x_r}{\sigma_{SL}\sqrt{2\pi}} \tag{6}$$

in which σ_{SL} is the empirical spreading parameter [38,39]. Assuming a thin shear layer gives $\sigma_{SL} = 13.5$.

By the inclusion of a stall criterion $f(\alpha, \alpha_c)$ and defining V_{SL} as zero, the relation C_{SL} corrects the blade sectional axial advance ratio when the blade section enters the shear layer region, that is, $R\sin(\theta) < y_{SL}(x)$:

$$C_{SL}(R,\theta) = 1 - f(\alpha,\alpha_c)h(R,\theta), \quad f(\alpha,\alpha_c) = \begin{cases} 0, & \alpha < \alpha_c \\ 1, & \alpha \geq \alpha_c \end{cases} \tag{7}$$

The axial inflow velocity $V_{ax}(R,\theta)$ is then found as the combination of the freestream, inviscid, and viscous contributions:

$$V_{ax}(R,\theta) = (\cos\alpha V_\infty + V_{\Gamma,x}(R,\theta))C_{SL}(R,\theta) \tag{8}$$

B. Tangential Inflow Velocity

The tangential inflow velocity is defined as the axial velocity. In this case, however, the vertical component $V_{\Gamma,y}$ of the wing's circulation is considered:

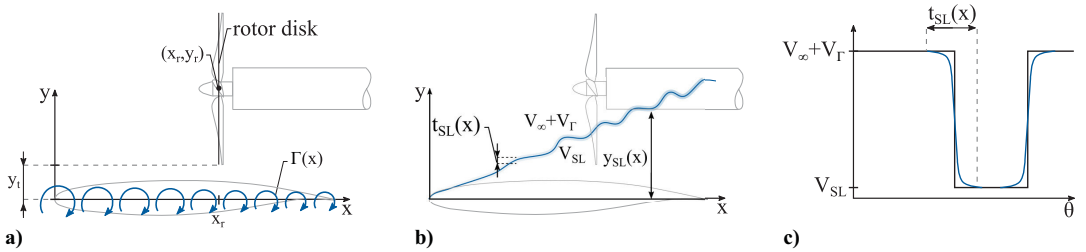

Fig. 3 Schematic of the modeling of the a) velocity increase by wing's circulation, b) the ingestion of the separated boundary layer, and c) variations in blade inflow velocity during a rotation through the shear layer.

$$V_{\Gamma,y}(R,\theta) = \frac{1}{2\pi}\int_0^c \frac{\Gamma(x)(x_r - x)}{(x_r - x)^2 + (y_r + R\sin\theta)^2}\,\mathrm{d}x \tag{9}$$

By the inclusion of the shear-layer correction term C_{SL}, the freestream velocity, and the rotational velocity of the blades, the tangential inflow $V_\theta(R,\theta)$ returns:

$$V_\theta(R,\theta) = \cos\theta(\sin\alpha V_\infty + V_{\Gamma,y}(R,\theta))C_{\mathrm{SL}}(R,\theta) + R\Omega \tag{10}$$

C. Unsteady Blade Loading

The inflow field is discretized in the azimuthal and radial directions to obtain the rotor loads. The step size should be sufficiently small to model the blade transitioning into the separated flow region, that is, $\Delta\theta < t_{\mathrm{SL}}/R_1 \approx 0.01\pi$. For each azimuthal position of the blade in the nonuniform flowfield, the loads are computed using Blade Element Momentum Theory (BEMT) [40]. This gives a distribution of local blade lift and drag coefficients, that are transformed to the frequency domain, resulting in $\hat{C}_{L,\mathrm{QS}}$ and $\hat{C}_{D,\mathrm{QS}}$.

Then, following a similar approach as in the work of van Arnhem et al. [18], a correction for unsteady effects is applied (reducing the amplitude and causing a phase delay), by multiplication of the complex local lift $\hat{C}_{L,\mathrm{QS}}$ coefficient by the Sears function $\hat{S}$ [41]:

$$\hat{C}_L(R,\sigma) = \hat{C}_{L,\mathrm{QS}}(R,\sigma)\hat{S}(R,\sigma) \tag{11}$$

In Eq. (11), σ is the reduced frequency that defines the degree of unsteadiness of the aeropropulsive forces, given by the loading harmonic n, the local blade chord c_b, and the induced velocity of the isolated rotor V_{iso}:

$$\sigma = \frac{n\Omega c_b}{2V_{\mathrm{iso}}} \tag{12}$$

D. Helicoidal Surface Theory

The complex blade sectional lift and drag coefficients are used as an input to predict the rotor noise emission, using helicoidal surface theory. This model was developed by Hanson [27] and extended [42] to include unsteady loading effects. For the mth noise harmonic and nth loading harmonic, the complex-valued pressure amplitude for the thickness-, lift-, and drag noise components are approximated by Eq. (13):

$$\begin{Bmatrix} P_{Vmn} \\ P_{Lmn} \\ P_{Dmn} \end{Bmatrix} = -\frac{2R_1\rho c_0^2 B\sin\theta_o}{8\pi y(1 - M_x\cos\theta_o)} e^{imB\left(\frac{\Omega R_1}{c_0} - \frac{\mathrm{sign}(m)|mB-n|\pi}{2}\right)}$$
$$\times \int_{R_0/R_1}^1 M_r^2 e^{i(\varphi_0+\varphi_s)}\hat{J}_{|mb-n|}\left(\frac{|m|BRM_t\cos\theta_o}{1 - M_x\cos\theta_o}\right)\begin{Bmatrix} k_x^2\hat{t}_{b,n}\psi_{V,n} \\ ik_y\frac{\hat{c}_{L,n}}{2}\psi_{L,n} \\ ik_x\frac{\hat{c}_{D,n}}{2}\psi_{D,n} \end{Bmatrix}\mathrm{d}R \tag{13}$$

In Eq. (13), $\hat{C}_{L,n}$ and $\hat{C}_{D,n}$ are the nth complex lift and drag coefficient; ψ_{Vn}, ψ_{Ln}, and ψ_{Dn} denote the spatial distribution of the volume, lift, and drag surface sources for each loading harmonic. For the lift and drag surface forces, a parabolic distribution over the blade section chord is assumed, which resembles the pressure distribution at large angles of attack.

The thickness sources term ψ_{Vn} is determined by the normalized thickness of the displaced fluid along the blade $H(X)$ [in which X is the normalized blade chord coordinate from $-1/2$ (leading edge) to $1/2$ (trailing edge)]. At large angles of attack, the flow can separate at a given chordwise X_s over the blade; see Fig. 4a.

The separation point X_s is approximated by a bipolar linear function of the current angle of attack of the blade section α, the angle at which the flow separates at the trailing edge α_0 and at the leading edge α_1:

$$X_s(\alpha,\alpha_0,\alpha_1) = \max(\min(X_1, f), X_0), \quad f = \frac{(\alpha_1 - \alpha)(X_0 - X_1)}{\alpha_0 - \alpha_1} \tag{14}$$

The values of α_0 and α_1 were found to be 10° and 2°, respectively, for the considered blade geometry and operating conditions.

Because of the variations in blade angle of attack during a rotation, $H(X)$ also varies along the azimuth. Consequently, the thickness noise spatial distribution ψ_{Vn} is found by integration of the Fourier transform of $H(X)$:

$$\psi_{Vn} = \int_{-1/2}^{1/2} \widehat{H}_n(X)e^{ik_xX}\,\mathrm{d}X \tag{15}$$

For the case of the isolated rotor, without interference with the airfoil, the computed loads and the tonal noise predictions were compared with experimental data, which showed good agreement (see Appendix C) validating the computational chain.

Figure 5 shows a decomposition of rotor noise in its thickness and loading noise component for the first blade-passing frequency harmonic of the isolated rotor for an advance ratio of $J = 0.3$ and $J = 0.6$. This shows that in upstream directions, that is, $90° < \theta_o < 270°$, the thickness noise is dominantly contributing, whereas in the downstream direction, loading noise exceeds the thickness noise.

To account for the reflection of acoustic waves by the wing's surface, the image-source model [43] is included. In this approach, a second noise source is mirrored along the (x, z) plane and translated to a vertical position of $y = -y_r$. The predicted tonal noise of the integrated rotor is then the superposition of the original noise source [computed by Eq. (13)] and its mirrored counterpart; see Fig. 4b. In the current work, the vertical offset between the real and image rotor axis is approximately equal to one wavelength of the first blade-passing frequency ($2y_r/\lambda \approx 1.1$), indicating that constructive interference may lead to an increase in noise for the first and second blade-passing frequencies.

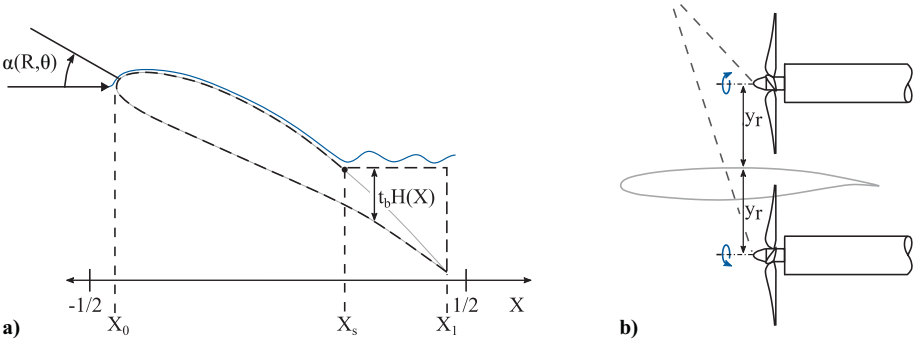

Fig. 4 Noise source model features: a) normalized blade thickness distribution $H(X)$ under large angles of attack and b) image-source model.

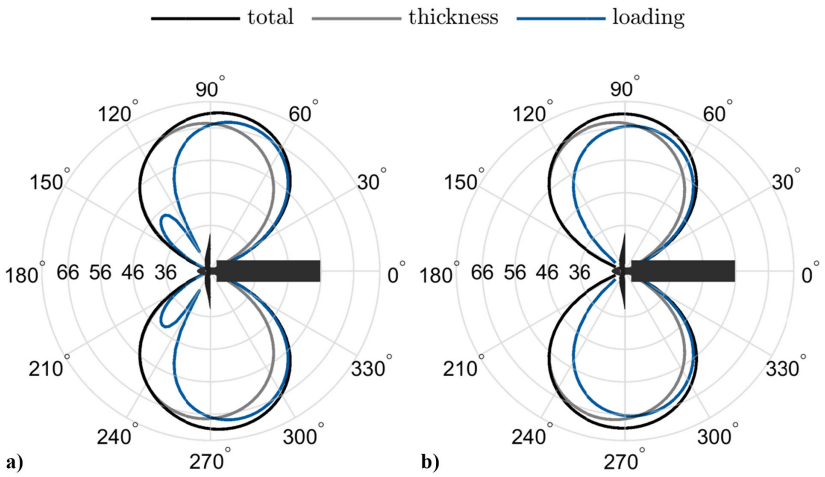

Fig. 5 Modeled directivity pattern of the first BPF of the isolated rotor for a) $J = 0.3$ and b) $J = 0.6$.

Note that application of the image-source model is only possible under restrictive conditions. First of all, the wing's chord should be larger than the wavelength of the first blade-passing frequency, which is met for the conditions in this study ($c/\lambda \approx 1.6$). Second, the image-source model does not hold when the rotor is operated close to an edge, due to diffraction of acoustic waves [5]. Because both the tip-gap ($0.27R_1$) and rotor–trailing-edge distance [$(c - x_r)/\lambda \approx 1.1$, for most of the concerned conditions] is large in the current work, such effects are not expected to occur. Nonetheless, analytical formulations are available to include such acoustic installation effects [5].

Finally, it is important to note that, by using the image-source model, only the noise above the rotor–wing system can effectively be predicted. The model does not consider the shielding properties or scattering effects of the wing, meaning that noise predictions below the pressure side of the wing are not included.

III. Experimental Validation

A. Setup and Wind Tunnel

The experiments were performed in the closed circuit Aeroacoustic Wind Tunnel Facility at the Royal Netherlands Aerospace Centre. The wind tunnel is positioned in an anechoic chamber ($9 \times 8 \times 6$ m), yielding an absorption rate of 99% above 200 Hz. A closed test section (95×95 cm^2) was used, limiting the turbulence intensity to a maximum of 0.01% at a freestream velocity of 20 m/s. To limit internal wall-to-wall reflections in the test section, the walls were fitted with acoustic transparent material over a 2 m length. The acoustic transmission losses through the walls are 2 dB over the frequency range of interest, and all experimental results were corrected for this.

B. Rotor and Wing Model

A DLR-F15 two-dimensional (2D) wing model was mounted vertically on a turntable in the floor of the closed test section, as schematically illustrated in Fig. 6. The chord of the wing is 240 mm, and transition was fixed at 10% chord by tripping the boundary layer on both the suction and pressure sides. A nacelle was positioned over the suction side of the wing and connected to the same turntable as the wing, with its axis aligned with the wing's chord direction. Inside the nacelle, a brushless inrunner motor is connected through two uniaxial FUTEK LSB205 thrust cells and a FUTEK QTA141 torque cell. The load and torque cells are excited by a single power supply with 7 V of direct current. Repeated measurements showed an average deviation of 4% for thrust and 0.6% for torque.

The inrunner motor drives a custom design six-bladed rotor (radius of 63.5 mm) at a constant shaft frequency of 383 Hz. The blade design of this rotor is based on a benchmarked version for low-Reynolds application derived from a NACA4412 airfoil. For additional details on the blade design, refer to the work of Grande et al. [44]. The rotor has been manufactured with computer numerical control (CNC) out of aluminum with 0.02 mm precision and cured to avoid material relaxation and oxidation. The test conditions are summarized in Table 1.

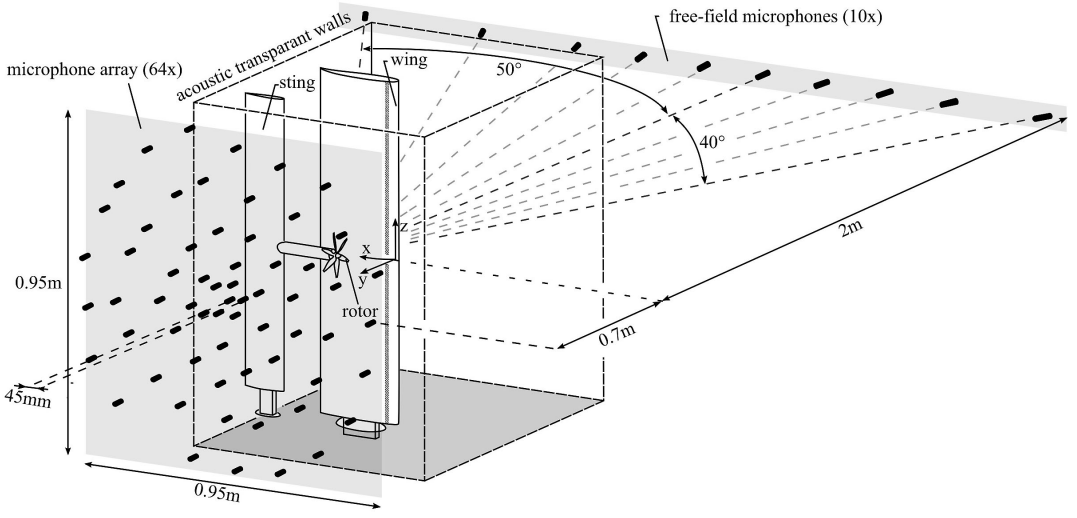

Fig. 6 3D schematic of the test section, microphone locations, and system of coordinates.

Table 1 Over-the-wing rotor system operating conditions

Wing chord c, mm	240
Aspect ratio AR	4
Shaft frequency, Hz	383
Number of blades B	6
Rotor radius R_1, mm	63.5
Rotor tip gap y_t/R_1	0.27
Rotor chord position x_r/c	[0.3, 0.6, 0.9]
Advance ratio J	[0, 0.3, 0.45, 0.6]
Angle of attack α	[−3, 0, 2, 4, 6, 8, 10, 11, 12, 13, 14, 15, 16, 20]
Wing chord Reynolds number Re_c	240,000–480,000
(3/4) R_1 rotor blade chord Reynolds number Re_{bc}	60,000
Tip Mach number M_t	0.42
Helmholtz number $He = \frac{2\pi c}{\lambda}$	10.11

Table 2 Illumination and imaging conditions

Seeding type	Di-ethyl-hexyl-sebacat
Particle relaxation time τ, μs	2
Illumination	Evergreen (200 mJ/pulse)
Sheet thickness dz, mm	3
Repetition rate, Hz	15
Camera type and resolution	2× Imager SCMOS CLHS (2560 px × 2160 px)
Stereo angle	35°
Objective focal length f, mm	50
Lens aperture $f_\#$	8
Optical magnification M	0.09
Field of view, cm^2	19 × 25
Number of recordings	300
Image analysis	Cross-correlation (32 px × 32 px, 75% overlap)
Vector pitch & resolution, mm	0.6 & 2.4

C. Acoustic Measurements

Acoustic measurements were performed outside of the test section, in the anechoic chamber. The noise of the rotor is measured using a microphone array consisting of 64 PCB 378A06 type microphones; see Fig. 6. The array was positioned at a distance of 0.7 m from the center of the test section and aimed toward the suction side of the wing. Ten free-field microphones, also of type PCB 378A06, record the sound from the pressure side of the wing to investigate the potential of noise shielding. The free-field microphones are positioned at a distance of 2 m from the center of the test section. The data acquisition was performed with a sampling frequency of 40.96 kHz and for a measurement duration of 20 s.

D. Aerodynamic Measurements

The inflow of the rotor is measured using stereoscopic particle image velocimetry (SPIV). For this, the acoustic transparent walls were replaced by optical transparent walls. A schematic of the SPIV setup is provided in Fig. 7a. The flow is seeded with DEHS (Di-Ethyl-Hexyl-Sebacat) tracer particles ($\tau = 2$ μs), which are illuminated by a Quantel Evergreen laser (200 mJ/pulse) in a sheet of 3 mm thickness. Illumination is performed at a rate of 15 Hz, and the duration for each pulse (pulse width) is $\delta t = 25$ ns. Recording is performed by two scientific Complementary Metal–Oxide–Semiconductor (sCMOS) cameras (Imager sCMOS CLHS) placed outside the section at a distance of 0.6 m from the center of the measurement region. The cameras are equipped with a 50 mm objective, set at numerical aperture $f_\# = 8$. The resulting field of view spans 19 cm × 25 cm ($3R \times 4R$). System synchronization is realized with a LaVision Programmable timing unit (PTU X), and each measurement comprises at least 300 recordings for a 20 s duration. An overview of the velocimetry measurement parameters is presented in Table 2.

The images were processed using an iterative multigrid method [45] with a final interrogation window size of 32×32 px^2 and an overlap of 75%. This resulted in a vector resolution of 9.6 mm and a vector spacing of 2.4 mm. The measurement uncertainty for the time-averaged velocity field is determined by the ratio between the relevant velocity fluctuations (magnitude of the standard deviations) and the square root of the number of statistically independent measurements. This results in an uncertainty of 0.0125% of the freestream velocity in the majority of the domain but locally increases to 3% in turbulent regions of the flow. At the same spanwise position as the velocimetry plane, a total of 59 orifices measure the static pressure over the wing's contour. The location of the span pressure taps is presented in Fig. 7c. The uncertainty of the static pressure measurement is determined by the spread in the data

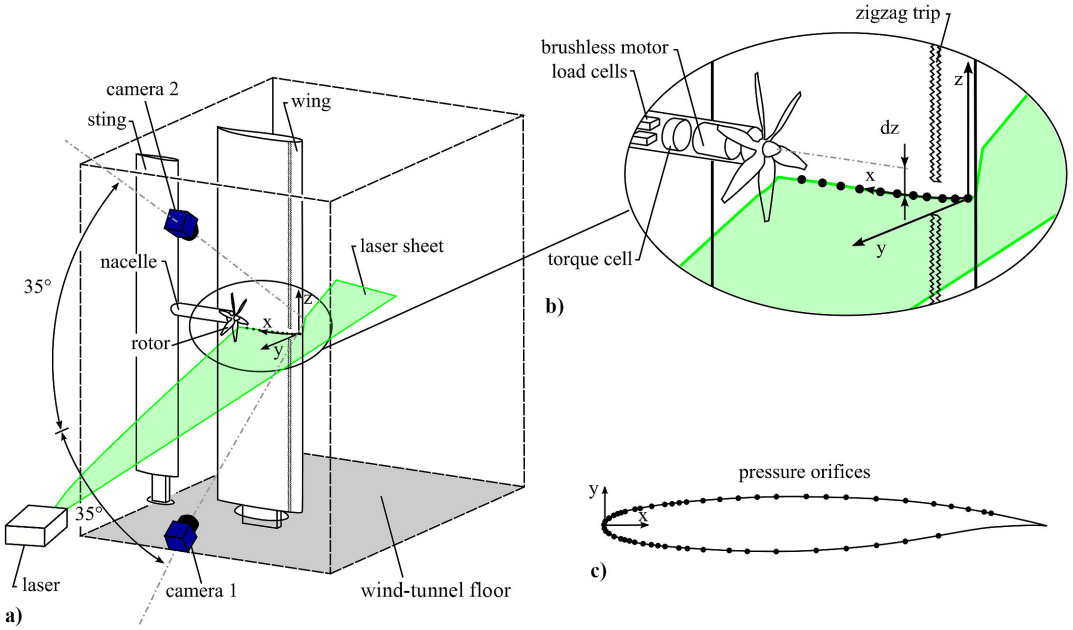

Fig. 7 Aerodynamic measurement setup: a) 3D schematic of the experimental apparatus and coordinate system; b) zoomed-in plot of the measurement techniques around the rotor, showing the translation in span direction by dz; and c) contour of the DLR-F15 wing model with location of the static pressure taps.

of the repeated measurements and was found to be $\pm 0.0125 C_p$. To enable time-averaged volumetric reconstruction of the velocity field and surface pressure reconstruction over the wing, the rotor is traversed in the span direction (dz in Fig. 7b) with a step size of 10 mm, covering a range of ± 50 mm ($0.8R_1$) in the z direction.

IV. Aeroacoustic Characteristics

The aeroacoustic properties of the over-the-wing rotor system will be elucidated by analysis of the experimental data. The difference in noise emission compared to the isolated rotor, the relative contributions of tonal and broadband noise, and the effect of varying operating conditions through the advance ratio and angle of attack are investigated. A fixed rotor position along the wing's chord of $x_r/c = 0.3$ is considered. The role of the rotor position on noise emissions is covered in more detail in Sec. V, along with a comparison to model predictions.

A. Installed Rotor Noise

The effect of the wing on the rotor noise is shown by comparison of the experimental data from the isolated and installed rotor. Noise spectra are generated using Welch's method by dividing the microphone data into blocks of 4096 samples with 50% overlap, yielding a frequency resolution of 10 Hz. Furthermore, a Hanning window is applied to mitigate spectral leakage, and all results are scaled to an observer distance of 1 m from the rotor hub. The noise spectra in the rotor plane ($\theta_O = \pm 90°$), obtained by bilinear interpolation of the SPL (sound pressure level, dB) values from the microphones, are presented in Fig. 8 for an advance ratio of $J = 0.6$, where a relatively low amount of thrust is provided by the rotor and $J = 0$, corresponding to hover conditions.

For cruise conditions (Fig. 8a), the results for the isolated rotor, shown by the solid gray lines, exhibit a dominant peak at the first BPF. The higher harmonics of the BPF show a strong reduction (greater than 20 dB) in sound pressure amplitude and fall below the broadband noise floor after the fourth harmonic. Note that also several weak spectral peaks occur at the shaft frequency (1/6th BPF) and its harmonics, attributed to a slight imbalance in the rotor–motor combination.

For the rotor-installed configuration, spectra are plotted for the suction side ($\theta_O = 90°$) and the pressure side ($\theta_O = 270°$). For the former, an increase in the tonal and high frequency (greater than 4 BPF) broadband noise levels is observed. The first BPF increases by approximately 3 dB, while the second and third harmonic attain up to 10 dB higher noise levels. On the pressure side, however, noise shielding by the wing reduces the first BPF with 10 dB. Furthermore, the high-frequency broadband noise is also lower when compared to the isolated rotor.

The dashed lines show the installation noise component, that is, the setup's noise emission without the rotor installed. Comparison of the spectra, and an analysis using noise source localization techniques [46,47], showed that low-frequency broadband noise ($f < 2$ BPF) for the installed configuration is dominated by an external noise source of the wind-tunnel configuration. Instead, for the high frequencies ($f > 3$ BPF), a moderate increase in broadband noise is observed when the rotor is active.

The overall noise level (OASPL) is obtained by integration of the spectra (without applying a frequency weighting filter) for the BPF and all frequencies exceeding $f \geq 2$ BPF. This frequency range is chosen to isolate the external noise source of the closed wind-tunnel configuration. The directivity pattern of the OASPL is plotted in Fig. 8b. At each of the observer angles on the suction side, the installed rotor shows larger values than the isolated rotor's data, in particular in the upstream direction ($\theta_O = 115°$). The OASPL values on the pressure side show a reduction in noise up to 5 dB, which is found in the downstream direction in particular. In the upstream direction ($\theta_O = 240°$), the shielding effect is limited because the isolated and installed configuration show a comparable value of the OASPL.

At hover conditions (Fig. 8c), the isolated rotor's tonal noise increases to 72 dB. Moreover, an elevation in broadband noise is apparent, which is attributed to flow separation occurring over a part of the span of the rotor blades near the root. The increase in the tonal noise by the insertion of the wing is more severe for $J = 0$ compared to the results of $J = 0.6$ (Fig. 8a). In particular, the higher harmonics exhibit a strong increase (greater than 15 dB). Moreover, the rotor harmonics for the installed condition are characterized by broadband humps in the neighboring frequencies, indicative of a

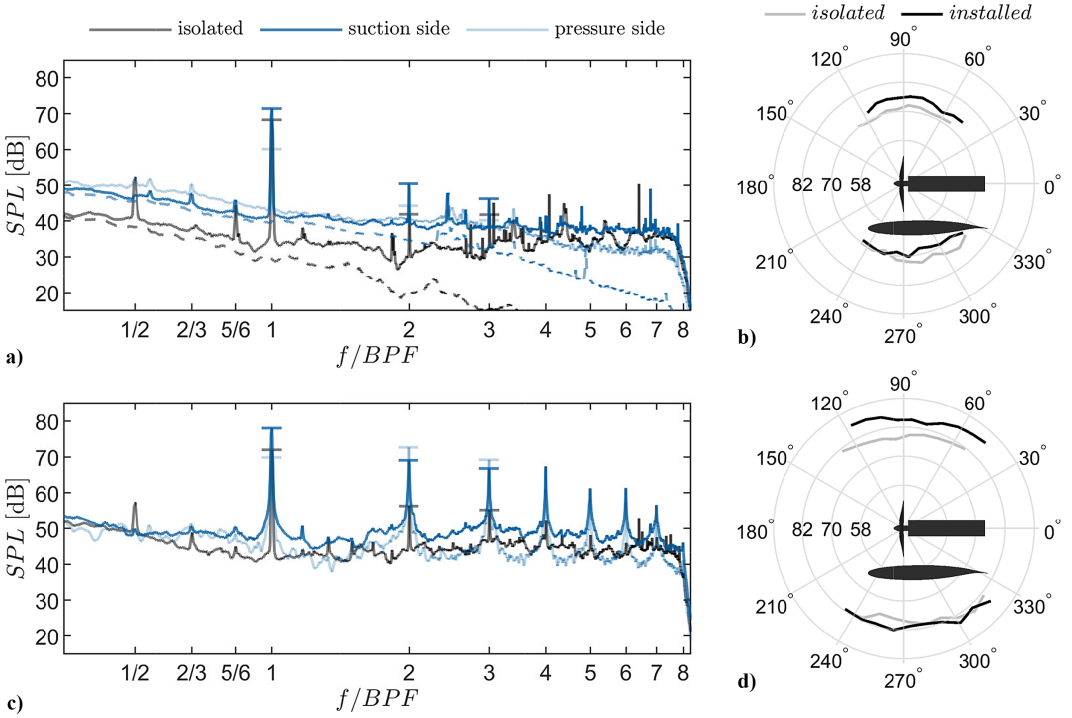

Fig. 8 Noise spectra in the rotor disk plane without inclination ($\alpha = 0°$) for a) $J = 0.6$ and c) $J = 0$ for $x_r/c = 0.3$. The horizontal lines in the spectra highlight the sound pressure levels of the first three blade-passing frequency harmonics. The dashed lines in the spectra of a) are the results with the rotor removed, and b) and d) show the directivity pattern of the OASPL (for $f =$ BPF $\cup$ [2 BPF, ∞)) for $J = 0.6$ and $J = 0$, respectively.

form of haystacking. While the tonal and broadband noise is reduced in the pressure side's direction, an unexpected increase of the second and third harmonics of the BPF compared to the suction side's value is seen here. Note that these harmonics are more sensitive to variations in inflow conditions and installation effects than the first BPF [48].

The noise directivity pattern in Fig. 8d shows more noise radiated in the forward direction ($\theta_O = 115°$) and backward ($\theta_O = 60°$) direction, due to the increase in broadband noise. Isolated and installed rotor's emissions in the wing's pressure side direction are comparable in magnitude for this advance ratio. The benefit of shielding is therefore negated by the increased rotor noise levels.

Installation effects are greater at hover ($J = 0$) conditions than at cruise conditions ($J = 0.6$). To explain the mechanism behind this, the measured velocity fields of the two conditions are presented in Figs. 9a and 9b. At the zero advance ratio, rotor thrust is higher, leading to a stronger pressure jump and contraction of the rotor disk stream tube. Consequently, the velocity field shows a region of flow reversal between the rotor and wing, as indicated by the streamlines below the rotor tip. The turbulent kinetic energy (TKE) in Figs. 9c and 9d reveal a great flow unsteadiness at the inflow of the rotor for $J = 0$, indicating intermittent separation of the wing's boundary layer. This explains the observed haystacking and elevated tonal components through blade–vortex interaction [22].

B. Effect of Angle of Attack

During transition from vertical to horizontal flight, angles of attack around stall are encountered. The effect of angle-of-attack on rotor noise is presented for a high ($J = 0.6$; see Figs. 10a and 10b) and low-advance ratio ($J = 0.3$; see Figs. 10c and 10d). One should note that the steady loads of the rotor are also affected by the inclination of the rotor system, but this falls outside the scope of the current work.

Inspection of Fig. 10a shows that the first BPF tone remains unaltered until $\alpha = 10°$. Broadband levels are dramatically elevated for $\alpha = 12°$, which marks the condition where the boundary layer of the wing separates near the leading edge. The first blade-passing frequency harmonic is reduced by 5 dB for this angle of attack.

The effect of angle of attack on noise directivity is presented in Fig. 10b by plotting the OASPL. No significant changes are exhibited, until reaching the stall angle. An increase in sound pressure level is observed in all directions but occurs most profoundly in the upstream radiation direction $\theta_O = 120°$.

Figure 10c shows the spectra for a reduced advance ratio ($J = 0.3$), where the rotor generates more thrust, representative of close-to-vertical flight conditions. In this case, for an angle of attack increase from $\alpha = 0°$ to $\alpha = 8°$, the BPF noise level exhibits a slight reduction, which can be attributed to decreased blade loading. At $\alpha = 10°$ and 12°, close to the wing's stall angle, an augmentation

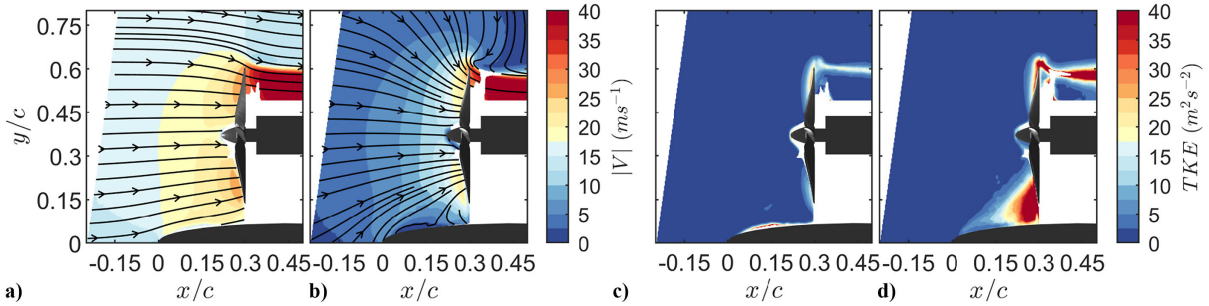

Fig. 9 Velocity magnitude contours $|V|$ and 2D velocity streamlines for a) $J = 0.6$ and b) $J = 0$ and turbulent kinetic energy TKE contours for c) $J = 0.6$ and d) $J = 0$.

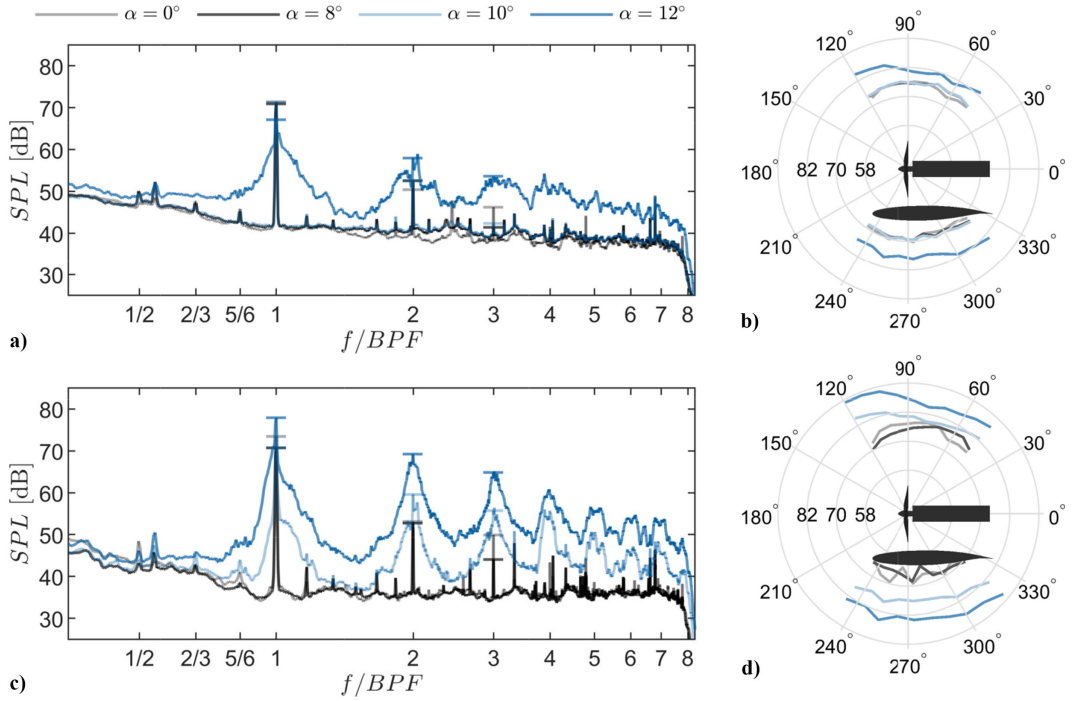

Fig. 10 Noise spectra in the rotor disk plane ($\theta_O = 90°$) for increasing inclination for a) $J = 0.6$ and c) $J = 0.3$ for $x_r/c = 0.3$ and b) and d) show the directivity pattern of the OASPL [for $f = \text{BPF} \cup [2\ \text{BPF}, \infty)$] for $J = 0.6$ and $J = 0.3$, respectively.

of the broadband noise around the BPF harmonics is seen. The OASPL directivity in Fig. 10d increased sound pressure levels in the upstream direction $\theta_O = 120°$ for these cases by turbulent ingestion.

To investigate the source mechanism of the observed spectra for $J = 0.3$, the flow topology and surface pressure are plotted for the various angles of attack in Fig. 11. The velocity magnitude and streamlines are extracted in the (x, y) plane, at an offset from the rotor hub of $dz = -0.2c$.

For $\alpha = 0°$ (Fig. 11a), the pressure distribution is mirror symmetric about $z = 0$ plane, where the absolute value of pressure is 25% higher in the midspan position compared to the edges of the domain. In the chordwise direction, a low-pressure region is found upstream, induced by the rotor. The velocity streamlines clearly show the contraction of the rotor's stream tube, both on the wing's surface and the extracted velocity field slice. By increasing the wing angle of attack, the flow accelerates over the suction side, and consequently, the static pressure over the wing decreases as is shown in Fig. 11b. The higher inflow velocity at the rotor disk leads to a decreased thrust, which is also manifested in a reduced contraction of the streamlines. The inclination of the rotor also results in an increase in thrust for the advancing side ($z < 0$) compared with the retreating side ($z > 0$) of the rotor disk. As a consequence, the pressure distribution exhibits mirror-asymmetry about the projected rotor axis.

Figure 11c for $\alpha = 10°$ shows a further reduction of the pressure in front of the rotor due to the flow acceleration around the leading edge. However, below and slightly in front of the rotor, a low-pressure region is found, entraining fluid from spanwise directions, which lifts upward and expels into the rotor disk. Consequently, the flow stagnates as it approaches the rotor and separates from the wing as indicated by the vertical velocity slices. The spatial extent of the reversed flow region is shown by the red isosurfaces. This shows that the air is primarily entrained from the positive span coordinate. Such flow topology creates a highly disturbed inflow, explaining the significant tonal noise increase.

A further increase in the angle of attack in Fig. 11d marks the early stages of stall for the used wing profile. In this case, the rotor's suction is not sufficient to delay the boundary-layer separation indicated by the higher surface pressures at the leading edge. Flow is entrained inside the separated boundary layer from spanwise and downstream directions toward a low-pressure region slightly upstream of the rotor. The reversed flow isosurfaces, in this case, are mirror symmetric around $z = 0$ and fill the area between the rotor disk and wing's surface. Note that the stagnation region due to the complex aerodynamic interaction between the rotor and the wing is not included in the proposed model.

C. Contributions of Tonal and Broadband Noise

It was shown that the presence of the wing alters both the tonal and broadband noise created by the rotor. Considering that the aeroacoustic model only computes the tonal noise, it is therefore valuable to examine the relative share of this to the overall sound pressure level. By computing phased-averaged noise spectra, the broadband noise is filtered out [49,50]. The tonal overall sound pressure level can then be computed by integration of the phase-locked spectra. Subsequently, the contribution of the broadband noise follows by subtracting the tonal noise from the microphone autopowers. The resulting tonal and broadband overall sound pressure levels in the rotor plane are presented in Fig. 12 as a functions of the angle of attack α.

From this follows that the tonal and broadband noise are within approximately 3 dB of each other in the prestall regime, for angles up to $\alpha = 10°$. A supplementary analysis using noise source localization techniques (not shown here for brevity) confirmed that rotor self-noise is the dominant broadband noise source under these conditions. For the lower advance ratio of $J = 0.3$, the rotor loads are higher, and therefore the contribution of tonal noise is greater

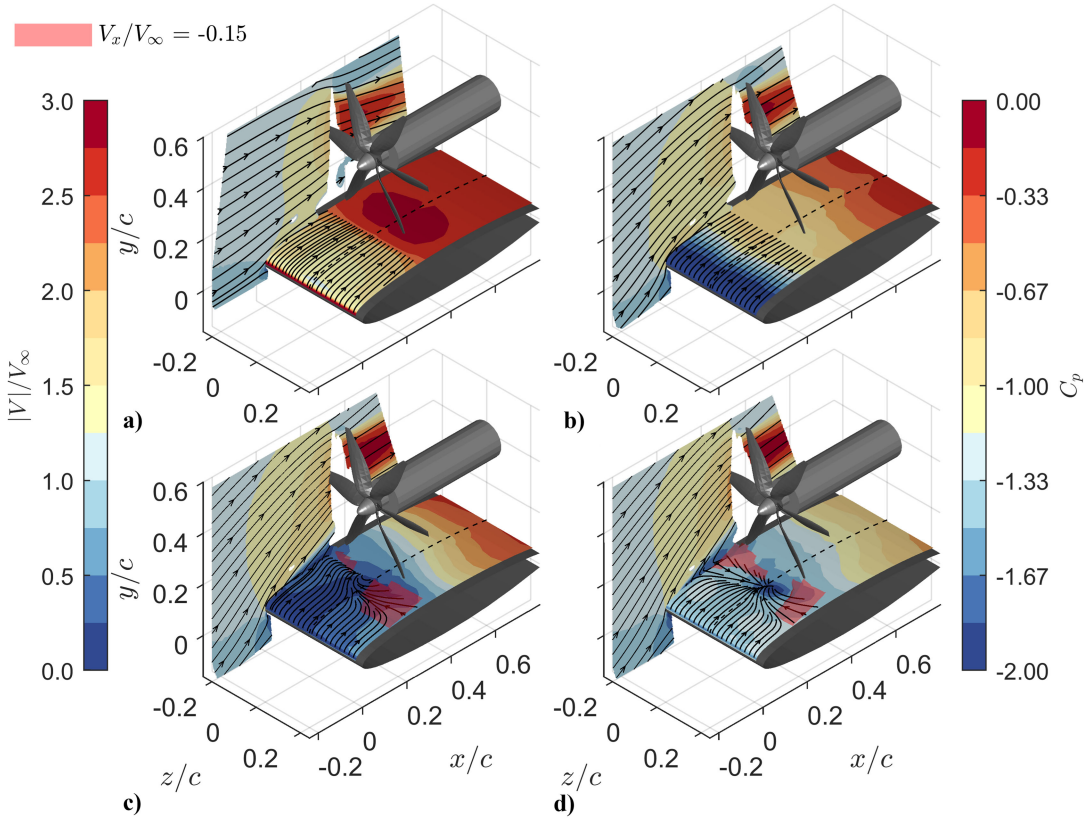

Fig. 11 Pressure coefficient C_p contours over the wing's surface in the (x, z) plane and projected 2D streamlines extracted at $dy = 0.025c$, normalized velocity magnitude $|V|/V_\infty$ and 2D velocity streamlines in the (x, y) plane at $dz = -0.2c$ and isosurfaces of streamwise velocity of $V_x = -0.15V_\infty$ for a) $\alpha = 0°$, b) $\alpha = 8°$, c) $\alpha = 10°$, and d) $\alpha = 12°$ for $x_r/c = 0.3$ and $J = 0.3$ (The dashes around V in the figure captions denote the magnitude of the velocity vector).

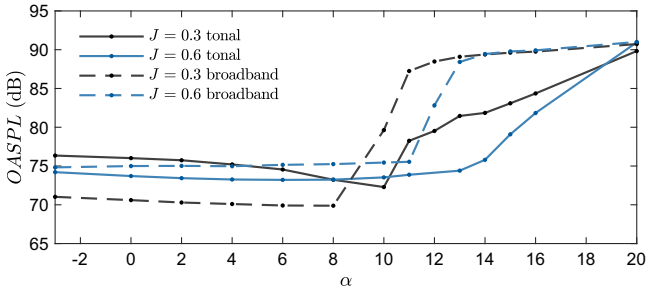

Fig. 12 OASPL in the rotor disk plane $\theta_O = 90°$ for $x_r/c = 0.3$, obtained by integration of the tonal and broadband spectra.

than that of broadband noise. For $J = 0.6$, the opposite is observed. As expected, the broadband noise becomes dominant in early stall conditions, leading to an increase in the order of 10 dB.

V. Model Results

In this section, the model predictions, which are limited to the tonal components, are compared to the measurements. This starts with a comparison of the wing-induced flowfield, which is used as a steady inflow distortion in the aeroacoustic chain.

A. Velocity Field

The experimentally obtained wing-induced flowfield is extracted from data of the isolated wing. The data are then sampled at the position of the rotor ($x_r = 0.3$) and decomposed in axial V_{ax} and azimuthal V_θ components, which are presented in Figs. 13a and 13b, respectively. The inflow velocities of the model, as defined by Eqs. (3) and (10) are presented in Figs. 13d and 13e, for the same conditions.

Both the experimental and modeled results show the expected increase in axial velocity compared to the freestream conditions, as shown in Figs. 13a and 13d. The model captures the axial velocity distribution with an overprediction in the magnitude of the wing-induced velocity by 10%. The measured and modeled azimuthal induced velocity by the wing are in good agreement, as is shown in Figs. 13b and 13e. The distribution shows an increase in azimuthal velocity on the advancing side and a reduction on the retreating side of the rotor.

The experiment inflow velocity of the installed configuration, with the rotor operated at $J = 0.3$, is presented in Fig. 13c. It is extracted upstream of the rotor disk at $x/c = 0.25$, approaching the disk being limited by the optical blockage of the blades. The combination of the steady inflow distortion of the wing and the rotor-induced flow generates velocity distribution that is maximized in the lower-left quadrant of the rotor disk and minimized in the top-right quadrant.

The model velocity distribution is the superposition of the predicted wing and the (nonuniform) rotor-induced flowfield. Note that the rotor-induced velocities from BEMT are solely defined at the rotor disk; hence, the predicted velocity field, as presented in Fig. 13f, is extracted at the rotor position of $x/c = 0.3$. To account for this, the contour levels have been corrected by a factor of 0.85 for the estimated stream tube contraction rate [10], based on the displaced extracted frame and the effective thickness of the rotor disk. The analytical axial induced velocity shows a similar distribution as the measurements (compare Fig. 13c and Fig. 13f), with extreme values in the lower-left and top-right quadrants. This validates the azimuthal variations in inflow conditions that are predicted in the model.

B. Rotor Loads

The wing-induced acceleration of the flow reduces the steady loads for the fixed-pitch rotor. The measured and predicted values of the rotor's thrust and torque coefficients are indicated by the markers for different advance ratios and varying angles of attack in Fig. 14. Here, the modeled steady thrust and torque are computed by averaging the loads over one rotor rotation and presented by the solid lines. A similar trend for thrust is captured by the model in Fig. 14a, although a slight underprediction up to 5% is observed. When the angle of attack of the rotor–wing system increases, the rotor's thrust is reduced due to the wing's circulation accelerating the flow toward the rotor. This effect is more pronounced when the advance ratio is increased. Beyond the isolated wing's stall angle of 12°, the thrust is increased, resulting from the ingestion of the low-momentum

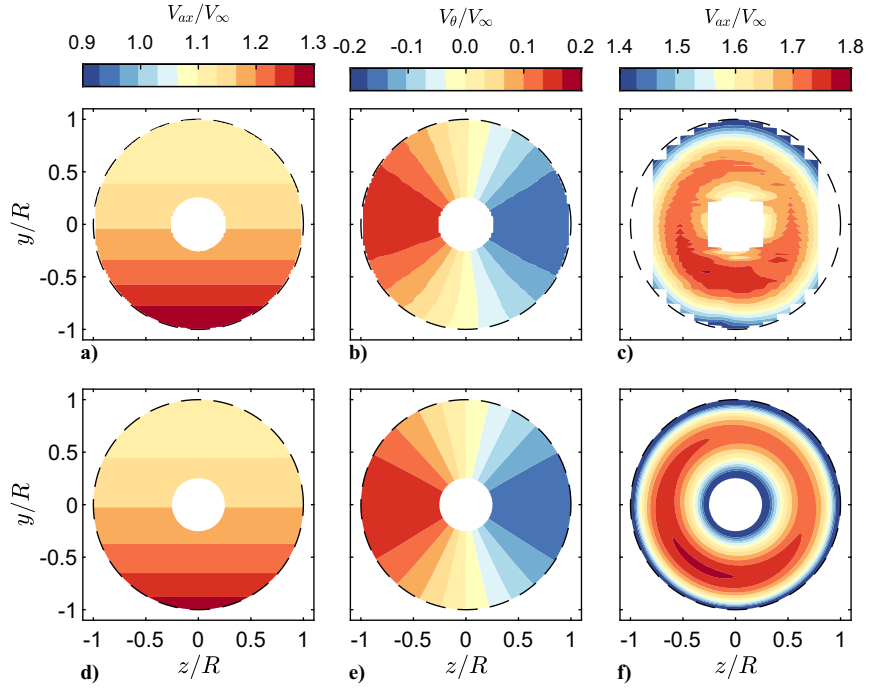

Fig. 13 Normalized velocities in the rotor plane for $x_r/c = 0.3$, $y_r/R_1 = 0.27$ and $\alpha = 8°$. The top row presents the experimental data of a) axial and b) azimuthal velocity of the isolated wing extracted at $x/c = 0.25$ and c) axial velocity of the rotor–wing system for $J = 0.3$ extracted slightly upstream of the disk at $x/c = 0.25$. The bottom row presents the model predictions for similar conditions.

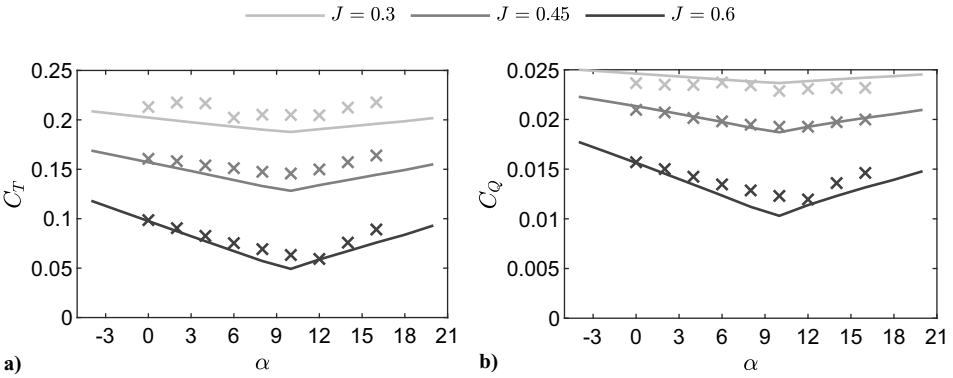

Fig. 14 Steady installed rotor's thrust coefficient C_T and torque coefficient C_Q as a function of the angle of attack for $x_r/c = 0.3$. The measurements are given by the markers, while the computed loads are shown by the solid lines.

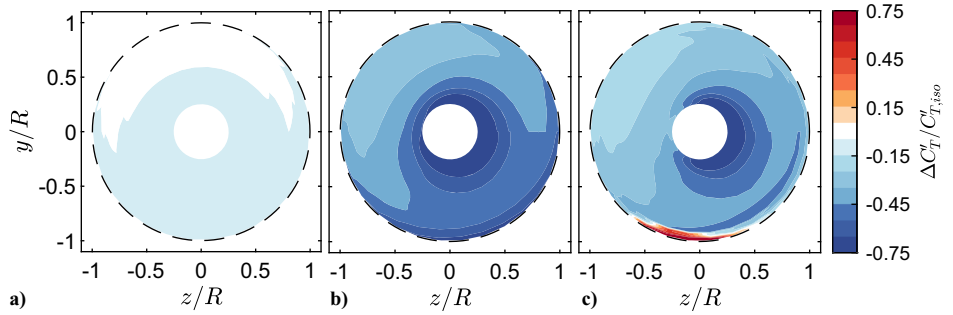

Fig. 15 Model predictions of the blade in-plane sectional thrust distribution with respect to an isolated rotor without inclination ($\Delta C'_T = C'_T - C'_{T,\text{iso}}$), for $x_r/c = 0.3$ and $J = 0.6$, for a) $\alpha = 0°$, b) $\alpha = 8°$, and c) $\alpha = 14°$.

boundary layer. The rotor's torque coefficient, as shown in Fig. 14b, shows a similar trend as the thrust curve. In this case, the model results provide a closer match to the measured values.

In Fig. 15, the predicted distribution of the thrust coefficient over the rotor disk, normalized by the isolated rotor thrust distribution, is presented for increasing angle of attack and an advance ratio of $J = 0.6$. For this advance ratio, the largest relative variations in thrust are expected from the model. An increase is observed in the variation of thrust along the azimuth with increasing angle of attack. For $\alpha = 8°$ in Fig. 15b, the thrust is reduced over the entire disk with a minimal value found in the lower right quadrant of the disk. However, the strongest variations in thrust are found for $\alpha = 14°$ in Fig. 15c. Here, the thrust partly recovers by the fact that the wing's circulation is reduced compared to $\alpha = 8°$. Moreover, for the current rotor position, a limited region of the boundary-layer ingestion on the lower side of the disk generates enhanced thrust levels. Such abrupt changes in thrust adversely affect the tonal components of the rotor's acoustics, which is shown in the following sections.

C. Noise Harmonics

To validate the model noise predictions, the experimental and modeled directivity patterns of the first BPF are presented in Fig. 16 for the same conditions as were presented in Fig. 15. Phased-locked spectra [49,50] are used in this case, strongly attenuating the broadband noise. For $\alpha = 0°$ and $\alpha = 8°$, in Figs. 16a and 16b, respectively, both the experimental and model results show the expected directivity pattern in which the emitted noise is maximized in the rotor disk plane, that is, $\theta_O = 90°$, and good agreement is obtained. Differences between modeled and measured values are below 2 dB over the greater part of measured directivity pattern. Some discrepancies are evident toward the downstream directions $\theta_O = 60°$ in Fig. 16b. The experimental results show strong variations with chordwise rotor position for this emission direction, and therefore the differences are associated with interference effects. A satisfactory resemblance between modeled and experimental results is found, showing a significant increase in tonal noise in forward and backward directions when the detached boundary layer is ingested (Fig. 15c).

The first three measured and modeled noise harmonics, relative to the isolated rotor at $\alpha = 0°$ ($\Delta\text{SPL} = \text{SPL} - \text{SPL}_{\text{iso}}$), are presented in Fig. 17 for $\alpha = 8°$ and $\alpha = 14°$. The modeled results without the inclusion of the image source are also presented here, to remove the effect of the reflection as assessed from simple geometrical acoustics (ray-theory) arguments.

Note that the experimental spectra of the isolated rotor could not be generated through phase averaging because the position of the shaft throughout acquisition was not available. Nonetheless, the broadband noise was found to have a negligible effect on the

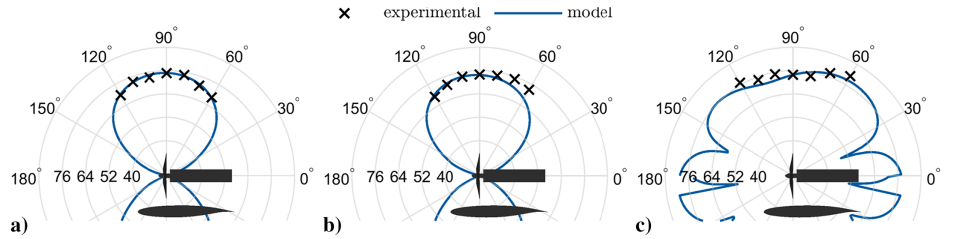

Fig. 16 Experimental and modeled directivity patterns of the first BPF of the installed rotor for $x_r/c = 0.3$ and $J = 0.$, for a) $\alpha = 0°$, b) $\alpha = 8°$, and c) $\alpha = 14°$.

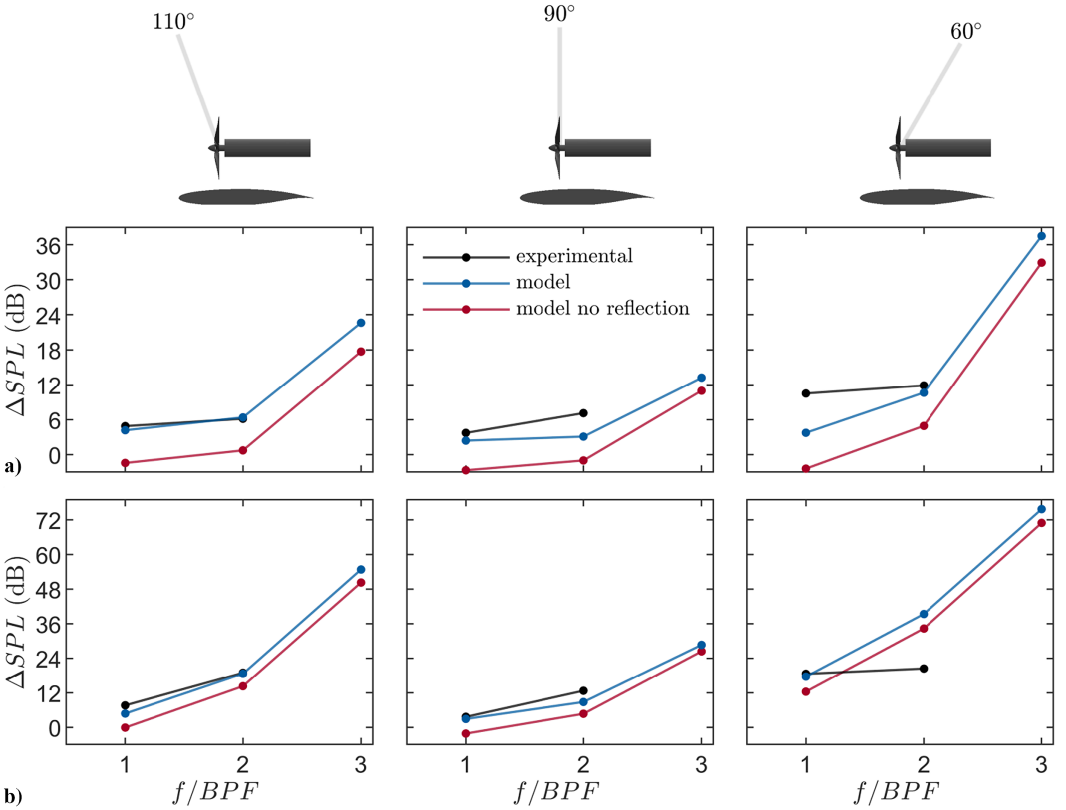

Fig. 17 Difference between the tonal components of the installed rotor and the isolated rotor at $\alpha = 0°$ (i.e., $\Delta\text{SPL} = \text{SPL} - \text{SPL}_{\text{iso}}$) for $x_r/c = 0.3$ and $J = 0.6$ in which a) $\alpha = 8°$ and b) $\alpha = 14°$.

amplitude of the first two blade-passing frequency harmonics for the isolated rotor. Despite that, generating spectra without phase averaging reduces the tonal amplitudes due to small variations in rotational velocity during acquisition. This loss was found to be a constant 2 dB (results presented in Appendix D), and all isolated rotor spectra have been corrected for this when computing the ΔSPL.

For $\alpha = 8°$ in Fig. 17a, in the disk plane (center column), the experimental results show an increase in the SPL of the first and second BPF by 3 and 7 dB, respectively, compared to the isolated rotor. The model (blue line) shows a similar elevation of the harmonic noise levels and predicts the values within an accuracy of 3 dB. Moreover, the model predicts a stronger effect on the third harmonic, which is increased by 14 dB. Reliable experimental values for this frequency have not been obtained due to the presence of broadband noise in the isolated rotor's spectral values.

The predicted effect of the reflection due to the presence of the wing is evaluated by comparison of the red (rotor aerodynamic noise) and blue line (rotor aerodynamic noise and reflection). It is clear that the first and second BPF are primarily elevated due to the reflection because the installed rotor's aerodynamic noise is in fact slightly lower (less than 1 dB) than that of the isolated rotor due to the reduction in steady loads. The third harmonic, however, exhibits a stronger dependence on the wing's aerodynamic effect, where the aerodynamic noise is increased by 7 dB compared to the isolated rotor. When considering up- and downstream observer positions (left and right columns of Fig. 17a), effects due to unsteady loading are expected to be more pronounced. This is reflected in the model results by a noticeable increase in the second and third blade-passing frequency harmonics. A good match between experimental results and predictions is found, except for an underestimation of the first BPF by approximately 8 dB for $\theta_O = 60°$. For poststall conditions (Fig. 17b), ΔSPL values for the second and third harmonics are elevated compared to the attached flow conditions. Similar results are again found for the experimental results and model predictions, with discrepancies below 3 dB for most of the results. However, a signification overprediction is present for $\theta_O = 60°$, for the second blade-passing frequency.

Figure 18 compares the rotor noise that is radiated over the suction side (black solid line) with the noise that is radiated toward

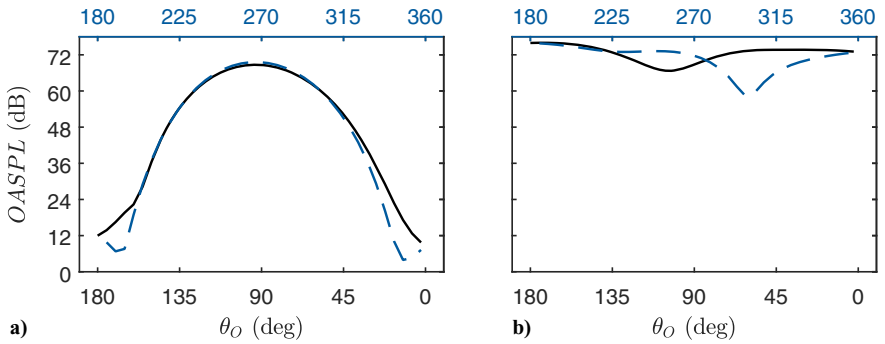

Fig. 18 Comparison between the modeled OASPL (obtained from the first three BPF harmonics) over the suction (with the exclusion of reflections) and pressure side for $x_r/c = 0.3$ and $J = 0.6$ in which a) $\alpha = 8°$ and b) $\alpha = 14°$.

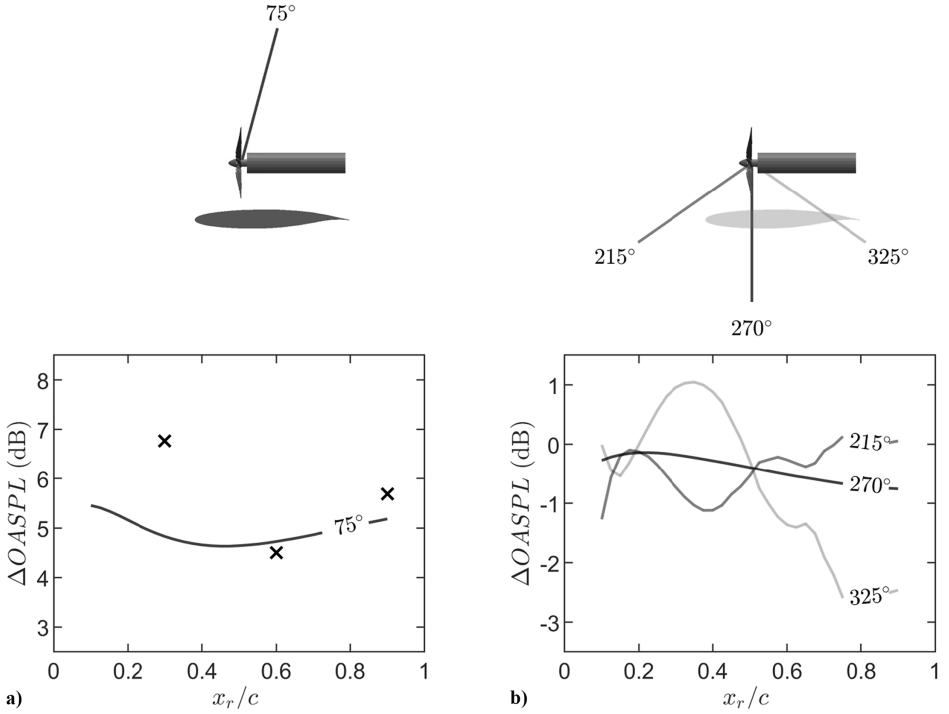

Fig. 19 Predicted tonal ΔOASPL levels with respect to the isolated rotor (for $\alpha = 0°$), for $\alpha = 8°$ and $J = 0.6$: a) results for $\theta_O = 75°$ in which the markers show the experimental results (obtained from the first three BPF harmonics) averaged over $\theta_O = 75 \pm 5°$ and b) the predicted values on the pressure side of the wing, in which only the aerodynamic effect of the wing is considered.

the pressure side of the wing (blue dashed line). Only the aerodynamic effect of the wing is accounted for here, that is, reflections from the image-source model are excluded. For $\alpha = 8°$, in Fig. 18a, the discrepancies between radiated noise toward the upper and lower sides are restricted to angles close to parallel to the rotor axis in downstream direction. In contrast, Fig. 18b illustrates that when the rotor ingests the shear layer such discrepancies are primarily observed closer to the rotor disk plane. Notably, local noise minima are found around $\theta_O = 60°$ and $\theta_O = 250°$.

D. Effect of Rotor Positioning

So far, a fixed rotor position of $x_r/c = 0.3$ was considered. To investigate the effect of rotor positioning along the wing's chord, the OASPL, generated from the first three blade-passing frequency harmonics, are presented in Fig. 19 for $\alpha = 8°$. This is performed for different observer angles downstream of the rotor disk.

The result for $\theta_O = 75°$ is presented in Fig. 19a. The experimental data for this observer angle are shown by the markers. While the model underestimates the tonal noise increase for the forward-positioned rotor by 1.5 dB, both model and experimental data show that the tonal noise is minimized for a midchord positioned rotor for this emission direction. This can be explained by the fact that the rotor's steady loads in the prestall regime are higher for a more aft-mounted rotor [20], while the variation in loading along the azimuth typically decreases through the circulation distribution along the wing's chord. Nonetheless, as was shown in Fig. 17, the increase in noise for observer positions near the disk plane is primarily the result of constructive interference, and therefore variations with chordwise positioning are limited.

More relevant is to investigate the rotor noise that is radiated toward the wing. Predictions for such observer angles are presented in Fig. 19b. In this case, the image source below the wing is removed; hence, only the aerodynamic effect of the wing on the rotor noise is considered. The result in the rotor disk plane ($\theta_O = 270°$) shows a reduction between 0 and 1 dB with respect to the isolated rotor. However, note that the steady loads of the rotor are also reduced up to 35% for these operating conditions. While variations with rotor position are marginal, tonal noise variations are slightly enhanced for a front-mounted rotor.

The effect of the unsteady loading (and therefore rotor positioning) is increased by considering directivity angles closer toward the direction of the rotor shaft, for example, $\theta_O = 325°$. These results show a maximization of the noise for a rotor positioned around 40% chord with variations up to 4 dB. The data of $\theta_O = 215°$ show an observer direction at which the thickness noise outweighs the loading noise for the used rotor geometry (recall Fig. 5). In this direction, variations with chord position are lower again because the effect of unsteady loading is suppressed.

VI. Conclusions

A model for the steady inflow distortion of over-the-wing mounted rotors is proposed. The model is applicable to rotors positioned over thin wings, with tip gaps exceeding the wing's boundary layer and without unsteady aerodynamic interferences (such as closely spaced rotor arrays). The modeled flow field and predicted noise signature have been validated using experimental aerodynamic and acoustic data of a single over-the-wing mounted rotor. The presented findings are therefore valuable to the understanding of the aerodynamic noise sources and the formulation of design guidelines for over-the-wing mounted rotors.

The modeled steady inflow distortion and distribution of the rotor-induced flow field correspond to that of the aerodynamic measurements. The resulting rotor loads in the prestall regime show a reduction in thrust for each blade sectional position with respect to the isolated rotor. Nonetheless, gradual variations in loading along the blade's azimuth are found, which depend on the geometric angle of attack and rotor position with respect to the wing. In these conditions, the model predictions and experimental results both show a similar increase (3–7 dB) of the tonal noise of the first two blade-passing frequency harmonics with respect to the isolated rotor, for observer positions in the rotor disk above the wing. The model predictions show that the tonal noise due to unsteady loading is minimal for these emission angles, and the observed increase in sound pressure level is primarily due to the reflections from the wing. Instead, the third harmonic exhibits a greater dependency on the aerodynamic effect of the wing and is elevated up to 14 dB. Although the wing reflects the noise of the rotor at the suction side, the measurements show a reduction in

tonal noise up to 10 dB and the broadband noise floor with respect to the isolated rotor below the wing. In poststall conditions, more rapid variations in rotor loads along the azimuth are found, during which the wing's shear layer is ingested. This results in a stronger elevation of the tonal components around the wing's suction side in the normal direction, up to 12 dB for the first two blade-passing harmonics.

A parametric study of the experimental results and model predictions, for prestall conditions, shows that tonal noise above the rotor is minimized for a midchord rotor position. For emission directions downstream, where the effects due to unsteady loading are more pronounced, the model predicts a maximum noise for a rotor positioned at 40% chord and variations with rotor positioning of up to 4 dB.

Although the model accurately captures the trend behavior with rotor positioning, discrepancies exist between predicted and measured noise values in the downstream direction, where unsteady loading effects are more pronounced. Moreover, the experimental results show that for low-advance ratios and angles of attack close to the wing's stall angle, the intermittent formation of a flow-reversal region between the rotor and wing leads to an additional increase in rotor noise by blade–vortex interaction. Such effects are not included in the model which explains part of the observed underestimates.

Appendix A:

A.1. Exact Terms of Induced Velocity by Circulation

The exact expressions for $V_{x,\Gamma}(R,\theta)$ and $V_{\Gamma,y}(R,\theta)$ can be obtained by integration of Eqs. (3) and (9), respectively. After integration, the result can be found in Eqs. (A1) and (A2):

$$V_{\Gamma,x}(R,\theta)=\frac{3c_l V_\infty}{8\pi c^2}\left(x_r(y_r+R\sin\theta)\,\ell_n\left(\frac{x_r^2+(y_r+R\sin\theta)^2}{(c-x_r)^2+(y_r+R\sin\theta)^2}\right)+(x_r^2-(y_r+R\sin\theta)^2-c^2)\left(\tan^{-1}\left(\frac{x_r-c}{(y_r+R\sin\theta)}\right)-\tan^{-1}\left(\frac{x_r}{(y_r+R\sin\theta)}\right)\right)-(y_r+R\sin\theta)c\right) \tag{A1}$$

$$V_{y,\Gamma}(R,\theta)=\frac{3c_l V_\infty}{16\pi c^2}\left(\left(c^2-x_r^2+(y_r+R\sin\theta)^2\right)\times\ell_n\left(\frac{x_r^2+(y_r+R\sin\theta)^2}{(c-x_r)^2+(y_r+R\sin\theta)^2}\right)+4x_r(y_r+R\sin\theta)\left(\tan^{-1}\left(\frac{x_r-c}{(y_r+R\sin\theta)}\right)-\tan^{-1}\left(\frac{x_r}{(y_r+R\sin\theta)}\right)\right)+2x_rc+c^2\right) \tag{A2}$$

A.2. Isolated Rotor Loads Validation

The measured and modeled isolated rotors thrust and torque coefficients are presented in Fig. A1. The model captures the general shape of the isolated rotor's performance trends and predicts the thrust and torque with sufficient accuracy. Some discrepancies are found for the thrust predictions, but these fall within or are close to the experimental uncertainty.

A.3. Isolated Rotor Tonal Noise Validation

The modeled tonal components of the isolated rotor are presented together with the isolated rotor spectra in Fig. A2a. The noise spectra are generated using Welch's method by dividing the microphone data

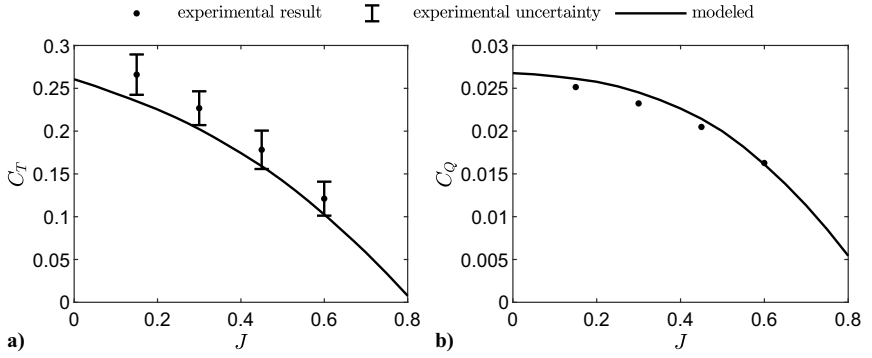

Fig. A1 Modeled and measured isolated rotor's a) thrust coefficient C_T and b) torque coefficient C_Q as a function of the advance ratio J. The experimental uncertainty is based on the spread of repeated measurements.

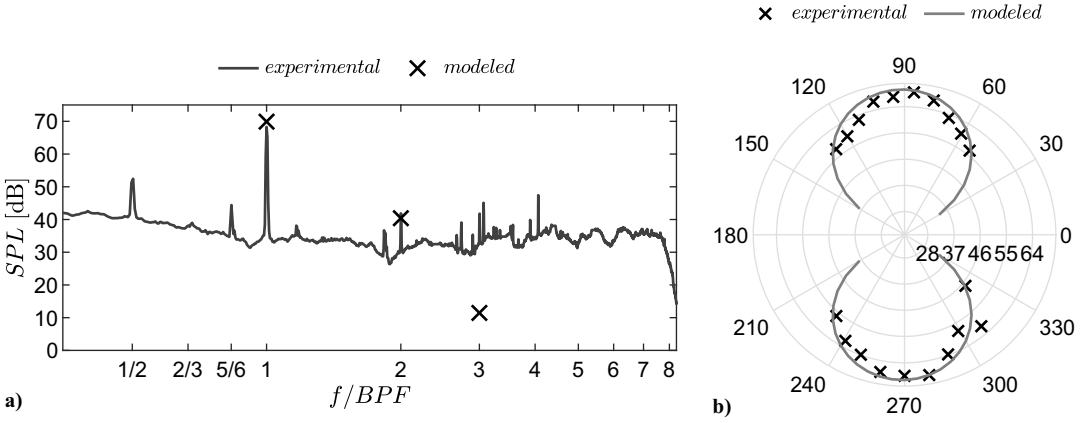

Fig. A2 Noise characteristics of the isolated rotor, showing a) experimental spectra and modeled tonal noise harmonics, and b) noise directivity of the first blade passing frequency (BPF).

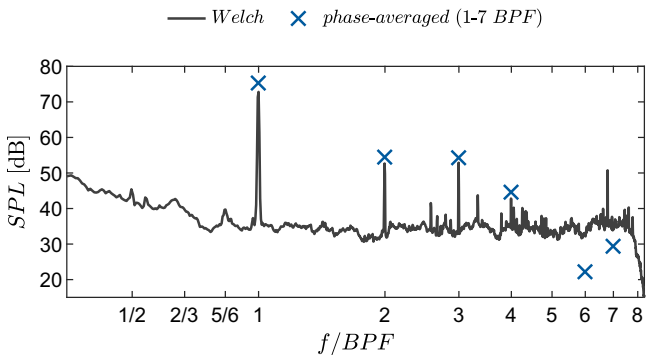

Fig. A3 Comparison between experimental tonal values obtained through Welch's method and phase-averaged spectra, for a microphone in the rotor disk plane ($\theta_O = 90°$) and $J = 0$, $\alpha = 0°$ and $x_r/c = 0.3$.

in segments of 2^{12} samples with 50% overlap, giving a frequency resolution of 10 Hz. This shows that the first two blade-passing frequency harmonics fall within an accuracy of 1.5 dB, while the model underpredicts the higher harmonics.

The directivity pattern of the first BPF in Fig. A2b shows the expected result for steady loading conditions for both the model prediction and experimental results, where the noise is maximized in the rotor plane. Discrepancies between the predictions and measurements reach a maximum of 3 dB for some observer directions.

A.4. Phase-Averaged Spectra

Spectra generated without phase averaging, that is, using a fixed sample count per window which is not synchronized with the rotor revolutions, can lead to reduced tonal amplitudes due to minor fluctuations in rotational velocity during data acquisition. This effect was observed by comparing the experimental phase-averaged tonal values with the acoustic spectrum as obtained using Welch's method, by dividing the same microphone data into segments of 2^{12} samples with 50% overlap. The results are presented in Fig. A3 and show a consistent reduction in tonal values for the first four BPF s of approximately 2 dB.

Acknowledgments

This research is funded by the European Union's Horizon 2020 research and innovation programme, under grant agreement number 860103, project ENODISE (Enabling Optimized Disruptive Airframe-Propulsion Integration Concepts). The authors would like to acknowledge Tim Deleij and Laurens de Haan for their assistance during the experiments and Tom Lanters for the design of the rotor mounting.

References

[1] Johnson, W., Silva, C., and Solis, E., "Concept Vehicles for VTOL Air Taxi Operations," *AHS Specialists Conference on Aeromechanics Design for Transformative Vertical Flight*, ARC-E-DAA-TN50731, American Helicopter Soc., 2018.

[2] Chauhan, S. S., and Martins, J. R. R. A., "Tilt-Wing eVTOL Takeoff Trajectory Optimization," *Journal of Aircraft*, Vol. 57, No. 1, 2020, pp. 93–112. https://doi.org/10.2514/1.C035476

[3] Thipphavong, D. P., Apaza, R., Barmore, B., Battiste, V., Burian, B., Dao, Q., Feary, M., Go, S., Goodrich, K. H., Homola, J., et al., "Urban Air Mobility Airspace Integration Concepts and Considerations," *2018 Aviation Technology, Integration, and Operations Conference*, AIAA Paper 2018-3676, 2018. https://doi.org/10.2514/6.2018-3676

[4] Zhong, S., Zhou, P., Chen, W., Jiang, H., Wu, H., and Zhang, X., "An Investigation of Rotor Aeroacoustics with Unsteady Motions and Uncertainty Factors," *Journal of Fluid Mechanics*, Vol. 956, 2023, Paper A16. https://doi.org/10.1017/jfm.2022.1097

[5] Acevedo Giraldo, D., Roger, M., Jacob, M. C., and Beriot, H., "Analytical Study of the Aerodynamic Noise Emitted by Distributed Electric Propulsion Systems," *28th AIAA/CEAS Aeroacoustics 2022 Conference*, AIAA Paper 2022-2830, 2022. https://doi.org/10.2514/6.2022-2830

[6] Cros, E., Roger, M., and Serre, G., "On the Very Low Frequency Scattering of Propeller Noise by a Neighboring Cylinder," *AIAA AVIATION 2021 FORUM*, AIAA Paper 2021-2251, 2021. https://doi.org/10.2514/6.2021-2251

[7] Lorenzoni, V., Tuinstra, M., Moore, P., and Scarano, F., "Aeroacoustic Analysis of a Rod-Airfoil Flow by Means of Time-Resolved PIV," *15th AIAA/CEAS Aeroacoustics Conference (30th AIAA Aeroacoustics Conference)*, AIAA Paper 2009-3298, 2009. https://doi.org/10.2514/6.2009-3298

[8] Sharma, S., Geyer, T. F., and Giesler, J., "Effect of Geometric Parameters on the Noise Generated by Rod-Airfoil Configuration," *Applied Acoustics*, Vol. 177, 2021, Paper 107908. https://doi.org/10.1016/j.apacoust.2021.107908

[9] Johnson, J. L., and White, R. E., "Exploratory Low-Speed Wind-Tunnel Investigation of Advanced Commuterconfigurations Including an Over-the-Wing Propeller Design," *Aircraft Design, Systems and Technology Meeting*, AIAA Paper 1983-2531, 1983. https://doi.org/10.2514/MASTM83

[10] Veldhuis, L., "Propeller Wing Aerodynamic Interference," Ph.D. Thesis, Delft Univ. of Technology, 2005.

[11] de Vries, R., "Hybrid-Electric Aircraft with Over-the-Wing Distributed Propulsion Aerodynamic Performance and Conceptual Design," Ph.D. Thesis, Delft Univ. of Technology, 2022.

[12] Broadbent, E., "Noise Shielding for Aircraft," *Progress in Aerospace Sciences*, Vol. 17, 1976, pp. 231–268. https://doi.org/10.1016/0376-0421(76)90009-9

[13] Vieira, A., Snellen, M., Malgoezar, A. M. N., Merino-Martinez, R., and Simons, D. G., "Analysis of Shielding of Propeller Noise Using Beamforming and Predictions," *Journal of the Acoustical Society of America*, Vol. 146, No. 2, 2019, pp. 1085–1098. https://doi.org/10.1121/1.5121398

[14] Beck, S. C., Müller, L., and Langer, S. C., "Numerical Assessment of the Vibration Control Effects of Porous Liners on an Over-the-Wing Propeller Configuration," *CEAS Aeronautical Journal*, Vol. 7, No. 2, 2016, pp. 275–286. https://doi.org/10.1007/s13272-016-0186-3

[15] Müller, L., Heinze, W., Kožulović, D., Hepperle, M., and Radespiel, R., "Aerodynamic Installation Effects of an Over-the-Wing Propeller on a High-Lift Configuration," *Journal of Aircraft*, Vol. 51, No. 1, 2014, pp. 249–258. https://doi.org/10.2514/1.C032307

[16] de Vries, R., and Vos, R., "Aerodynamic Performance Benefits of Over-the-Wing Distributed Propulsion for Hybrid-Electric Transport Aircraft," *Journal of Aircraft*, Vol. 60, No. 4, 2023, pp. 1201–1218. https://doi.org/10.2514/1.C036909

[17] de Vries, R., van Arnhem, N., Avallone, F., Ragni, D., Vos, R., Eitelberg, G., and Veldhuis, L. L. M., "Experimental Investigation of Over-the-Wing Propeller-Boundary-Layer Interaction," *AIAA Journal*, Vol. 59, No. 6, 2021, pp. 2169–2182. https://doi.org/10.2514/1.J059770

[18] van Arnhem, N., de Vries, R., Sinnige, T., Vos, R., Eitelberg, G., and Veldhuis, L. L. M., "Engineering Method to Estimate the Blade Loading of Propellers in Nonuniform Flow," *AIAA Journal*, Vol. 58, No. 12, 2020, pp. 5332–5346. https://doi.org/10.2514/1.J059485

[19] Petricelli, F., Chaitanya, P., Palleja-Cabre, S., Meloni, S., Joseph, P. F., Karimian, A., Palani, S., and Camussi, R., "An Experimental Investigation on the Effect of in-Flow Distortions of Propeller Noise," *Applied Acoustics*, Vol. 214, 2023, Paper 109682. https://doi.org/10.1016/j.apacoust.2023.109682

[20] Dekker, H. N., Tuinstra, M., Baars, W. J., Scarano, F., and Ragni, D., "Aero-Propulsive Performance Modelling of Over-the-Wing Propulsion at Incidence," *AIAA Journal (submitted)*, 2024, Paper J064985.

[21] Jamaluddin, N. S., Celik, A., Baskaran, K., Rezgui, D., and Azarpeyvand, M., "Experimental Analysis of a Propeller Noise in Turbulent Flow," *Physics of Fluids*, Vol. 35, No. 7, 2023. https://doi.org/10.1063/5.0153326

[22] Murray, H. H., Devenport, W. J., Alexander, W. N., Glegg, S. A. L., and Wisda, D., "Aeroacoustics of a Rotor Ingesting a Planar Boundary Layer at High Thrust," *Journal of Fluid Mechanics*, Vol. 850, 2018, pp. 212–245. https://doi.org/10.1017/jfm.2018.438

[23] Gutin, L., "On the Sound Field of a Rotating Propeller," *Physikalische Zeitschrit der Sowjetinion: Physical Magazine of the Soviet Union*, Vol. 9, No. 1, NACA-TM-1195, 1948, https://ntrs.nasa.gov/api/citations/20030068996/downloads/20030068996.pdf.

[24] Ffowcs Williams, J. E., and Hawkings, D. L., "Sound Generation by Turbulence and Surfaces in Arbitrary Motion," *Philosophical Transactions for the Royal Society of London. Series A, Mathematical and Physical Sciences*, Vol. 264, No. 1151, 1969, pp. 321–342. https://doi.org/10.1098/rsta.1969.0031

[25] Ffowcs Williams, J. E., and Hawkings, D. L., "Theory Relating to the Noise of Rotating Machinery," *Journal of Sound and Vibration*, Vol. 10, No. 1, 1969, pp. 10–21. https://doi.org/10.1016/0022-460X(69)90125-4

[26] Goldstein, M. E., *Aeroacoustics*, Mc Graw-Hill, New York, NY, 1976.

[27] Hanson, D. B., "Helicoidal Surface Theory for Harmonic Noise of Propellers in the Far Field," *AIAA Journal*, Vol. 18, No. 10, 1980, pp. 1213–1220. https://doi.org/10.2514/3.50873

[28] Brouwer, H., "Analytical Method for the Computation of the Noise from a Pusher Propeller," *16th AIAA/CEAS Aeroacoustics Conference*, AIAA Paper 2010-3848, 2010. https://doi.org/10.2514/6.2010-3848

[29] Roger, M., Acevedo-Giraldo, D., and Jacob, M. C., "Acoustic Versus Aerodynamic Installation Effects on a Generic Propeller-Driven Flying Architecture," *International Journal of Aeroacoustics*, Vol. 21, Nos. 5-7, 2022, pp. 585–609. https://doi.org/10.1177/1475472X221107372

[30] Roger, M., and Moreau, S., "Tonal-Noise Assessment of Quadrotor-Type UAV Using Source-Mode Expansions," *Acoustics*, Vol. 2, No. 3, 2020, pp. 674–690. https://doi.org/10.3390/acoustics2030036

[31] Moreau, S., and Roger, M., "Advanced Noise Modeling for Future Propulsion Systems," *International Journal of Aeroacoustics*, Vol. 17, Nos. 6-8, 2018, pp. 576–599. https://doi.org/10.1177/1475472X18789005

[32] De Prenter, F., Zarri, A., and Casalino, D., "Low-Cost Computational Modeling of Aeroacoustic Interactions Between Adjacent Propellers," *30th AIAA/CEAS Aeroacoustics Conference*, AIAA Paper 2024-3069, 2024. https://doi.org/10.2514/6.2024-3069

[33] Dekker, H., Brouwer, H., Kok, J., Laban, M., and Tuinstra, M., "Tonal Noise Measurements and Simulations of an Over-the-Wing Propeller," *AIAA AVIATION 2023 Forum*, AIAA Paper 2023-3358, 2023. https://doi.org/10.2514/6.2023-3358

[34] Okulov, V. L., Sørensen, J. N., and Wood, D. H., "The Rotor Theories by Professor Joukowsky: Vortex Theories," *Progress in Aerospace Sciences*, Vol. 73, 2015, pp. 19–46. https://doi.org/10.1016/j.paerosci.2014.10.002

[35] Tuck, E. O., "A Criterion for Leading-Edge Separation," *Journal of Fluid Mechanics*, Vol. 222, No. -1, 1991, p. 33. https://doi.org/10.1017/S0022112091000988

[36] Görtler, H., "Berechnung von Aufgaben der freien Turbulenz auf Grund eines neuen Näherungsansatzes," *ZAMM - Journal of Applied Mathematics and Mechanics / Zeitschrift für Angewandte Mathematik und Mechanik*, Vol. 22, No. 5, 1942, pp. 244–254. https://doi.org/10.1002/zamm.19420220503

[37] Sijtsma, P., Oerlemans, S., Tibbe, T. G., Berkefeld, T., and Spehr, C., "Spectral Broadening by Shear Layers of Open Jet Wind Tunnels," *20th AIAA/CEAS Aeroacoustics Conference*, AIAA Paper 2014-3178, 2014. https://doi.org/10.2514/6.2014-3178

[38] Champagne, F. H., Pao, Y. H., and Wygnanski, I. J., "On the Two-Dimensional Mixing Region," *Journal of Fluid Mechanics*, Vol. 74, No. 2, 1976, pp. 209–250. https://doi.org/10.1017/S0022112076001778

[39] Liepmann, H. W., and Laufer, J., "Investigations of Free Turbulent Mixing," NACA-TN-1257, 1947.

[40] Glauert, H., *Airplane Propellers*, Springer, Berlin, Heidelberg, 1935, pp. 169–360. https://doi.org/10.1007/978-3-642-91487-4_3

[41] Sears, W. R., "Some Aspects of Non-Stationary Airfoil Theory and Its Practical Application," *Journal of the Aeronautical Sciences*, Vol. 8, No. 3, 1941, pp. 104–108. https://doi.org/10.2514/8.10655

[42] Donald, B. H., "Noise of Counter-Rotation Propellers," *Journal of Aircraft*, Vol. 22, No. 7, 1985, pp. 609–617. https://doi.org/10.2514/3.45173

[43] Allen, J. B., and Berkley, D. A., "Image Method for Efficiently Simulating Small-Room Acoustics," *Journal of the Acoustical Society of America*, Vol. 65, No. 4, 1979, pp. 943–950. https://doi.org/10.1121/1.382599

[44] Grande, E., Romani, G., Ragni, D., Avallone, F., and Casalino, D., "Aeroacoustic Investigation of a Propeller Operating at Low Reynolds Numbers," *AIAA Journal*, Vol. 60, No. 2, 2022, pp. 860–871. https://doi.org/10.2514/1.J060611

[45] Scarano, F., and Riethmuller, M. L., "Iterative Multigrid Approach in PIV Image Processing with Discrete Window Offset," *Experiments in Fluids*, Vol. 26, No. 6, 1999, pp. 513–523. https://doi.org/10.1007/s003480050318

[46] Sijtsma, P., "Elements of Acoustic Array Data Processing," Tech. Rept. NLR-TR-2014-003, 2014.

[47] Chiariotti, P., Martarelli, M., and Castellini, P., "Acoustic Beamforming for Noise Source Localization - Reviews, Methodology and Applications," *Mechanical Systems and Signal Processing*, Vol. 120, 2019, pp. 422–448. https://doi.org/10.1016/j.ymssp.2018.09.019

[48] Beck, A. B., Cordioli, J. A., Bonomo, L. A., Fonseca, J. V. N., Simões, L. G., Tourinho, A. M., Casalino, D., Ragni, D., and Avallone, F., "Comparative Assessment of Isolated Propeller Noise Test Rigs," *30th AIAA/CEAS Aeroacoustics Conference*, AIAA Paper 2024-3323, 2024.

[49] Sijtsma, P., and Brouwer, H., "Deconvolution of Azimuthal Mode Detection Measurements," *Journal of Sound and Vibration*, Vol. 422, 2018, pp. 1–14. https://doi.org/10.1016/j.jsv.2018.02.029

[50] Rademaker, E., Sijtsma, P., and Tester, B., "Mode Detection with an Optimised Array in a Model Turbofan Engine Intake at Varying Shaft Speeds," *7th AIAA/CEAS Aeroacoustics Conference and Exhibit*, AIAA Paper 2001-2181, 2001. https://doi.org/10.2514/6.2001-2181

A. Jones
Associate Editor